Alma Mater Studiorum · Università di Bologna

Scuola di Scienze
Corso di Laurea Magistrale in Fisica del Sistema Terra

Scenarios of lateral collapses of the Vavilov seamount in the central Tyrrhenian Sea

Relatore:
Prof. Stefano Tinti

Correlatore:
Dott. Filippo Zaniboni

Presentata da:
Daniele Arcangeli

Sessione III
Anno Accademico 2017/2018

Acknowledgements

I would like to express my deep gratitude to Professor Tinti and Dr. Zaniboni, my research supervisors, for their patient guidance, enthusiastic encouragement and useful remarks of this research work. My grateful thanks are also extended to Dr. Gamberi and Dr. Marani that provided me the seismic data and helped me with their interpretation. I would also like to thank Professor Romagnoli for her contribution to the bibliographic research and Dr. Gallotti for his assistance.

I extend my thanks to Mati for the help in revising some sentences that sounded *"troppo italiane"* and to the friends of the association "l'Altra Babele" for the great time spent together.

Finally, I wish to thank my brother and my parents for their encouragement throughout my study.

Sommario

La forte asimmetria tra i fianchi del Vavilov, vulcano sottomarino situato nel mar Tirreno, potrebbe essere dovuta ad un collasso verificatosinel versante occidentale in epoca non recente. Nella tesi vengono studiati due scenari ciascuno con propria morfologia del versante occidentale pre-frana. Nello scenario 1 si assume che, al di fuori della nicchia di distacco, la superficie di scivolamento coincida con l'attuale fondale marino. Diversamente, nello scenario 2, si fa l'ipotesi che la differenza di profondità dei fondali a ovest (meno profondo) e a est (più profondo) del Vavilov sia dovuta alla presenza di materiale franato che è stato successivamente eroso e rielaborato dalle correnti marine e parzialmente ricoperto dai processi di sedimentazione. Di conseguenza, il fondale attuale viene scavato nello scenario 2 per determinare la superficie di scivolamento. Per quanto riguarda la ricostruzione del versante di frana, si procede in modo analogo allo scenario 1.

Il moto della frana è simulato tramite il modello UBO-BLOCK2 che è stato sviluppato dal gruppo di ricerca sugli tsunami dell'Università di Bologna. La frana viene schematizzata con una matrice di blocchi che scivolano su una superficie con attrito. I blocchi sono inoltre soggetti alle forze di interazione reciproca e alle forze resistive dovute al fluido in cui sono immersi. Per le simulazioni relative allo scenario 1 viene studiata l'influenza dei parametri del modello sui risultati. Nello scenario 2, l'accordo tra il deposito ipotizzato e quello simulato viene utilizzato per calibrare i parametri del modello, e in particolare per calibrare il coefficiente di attrito che è il parametro che maggiormente influenza la dinamica dei blocchi.

La conclusione più rilevante della tesi è che l'analisi dello scenario 2 dà sostegno in modo plausibile all'ipotesi che il versante occidentale del Vavilov sia franato e che la massa franata si sia depositata proprio ai piedi dell'edificio vulcanico con modesto run-out e che il deposito sia la causa dello squilibrio oggi evidente fra la profondità della piana abissale a ovest e a est del vulcano, con differenze nell'ordine di alcune centinaia di metri.

Abstract

The strong EW asymmetry observed for the Vavilov seamount could be the result of an ancient collapse from its western flank. Two scenarios for the pre-collapse morphology of the seamount are built up by reshaping the western flank of Vavilov and modelling it as the eastern one. In scenario 1 the detached mass is assumed to slide down on the present bathymetry, i.e. the sliding surface outside the detachment niche is identified with the today's abyssal plane to the west of Vavilov. Instead, in scenario 2 it is assumed that the difference between the depth of the western (less deep) and eastern (deeper) abyssal planes is due to the deposition and subsequent reworking of the collapsed material. Therefore, in scenario 2 the identified deposit is removed from the present bathymetry, while the western flank is reshaped approximately like in scenario 1.

The motion of the landslide is simulated by the model UBO-BLOCK2, developed by the Tsunami Research Team of the University of Bologna, that treats it as a grid of blocks sliding under the effect of friction, drag forces and interaction forces. The influence of various parameters on the model's output is discussed for simulations that regard scenario 1. For scenario 2, the agreement between the hypothesised deposit and the one computed through the simulations is used to tune the model parameters, and in particular the sea bottom friction coefficient, that is the one that most affects the landslide motion.

The conclusion of the thesis is that scenario 2 supports reasonably well the hypothesis that the Vavilov seamount experienced a collapse of the western flank, that the collapsed material filled the western abyssal plane causing an average decrease of the sea floor depth by hundreds of meters, that most of the material accumulated not too far from the feet of the Vavilov's seamount, which is consistent with the available seismic lines.

Contents

Chapter 1

The landslide problem

Introduction

The aim of this chapter is to give a concise overview from a physical point of view of the landslide problem and to introduce the phenomenon of water wave generation triggered by mass movements. Therefore, the chapter is divided in four sections: the first one is a brief description of the morphology and of the terminology used to describe a landslide. It is followed by the classification based upon types of movement as proposed by Cruden & Varnes [4], that is the topic of section 1.2. Section 1.3 is the analysis of landslide causes, that is conducted by invoking the Mohr Coulomb criterion. Lastly, the fourth section is about those mass failures that, interacting with water basins, are able to generate tremendous waves such as *tsunamis*.

1.1 Characteristics of Landslides

A brief description of landslides morphology is needed to discuss the landslide problem. For this aim we can refer to Fig. 1.1.

The landslide can be divided in two different zones: the *depletion zone* and the *accumulation zone*. The first one is the zone within which the collapsed material lies below the original ground surface, while in the latter it lies above.

The region adjacent to the highest part of the landslide is called *crown*, while *surface of rupture* stands for the surface on which the sliding takes place. The part of the surface of rupture left uncovered by the main body is usually characterised by its steepness and is called *main scarp*. During the sliding the main body can be affected by other minor slides that originate *minor scarps*. The *foot* is the material deposited beyond the surface of rupture, and the farthest deposit point from the crown is the *tip*. Laterally a landslide is delimited by the *flanks*.

The following geometrical quantities are used to characterise the landslide:

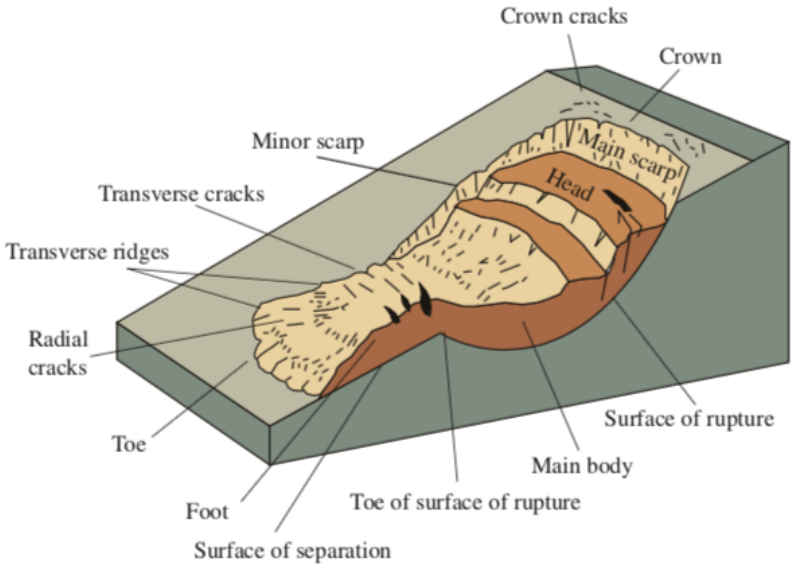

Figure 1.1: An idealised landslide showing commonly used nomenclature for its parts. [Credit to USGS [18]]

- Total length, L: the minimum length from the tip of the landslide to the crown
- Total width, W: the distance from one flank to the other
- Total depth D: the maximum vertical length from the landslide summit to the sliding surface

1.2 Types of movement

The landslides are classified on the base of the material involved and of the type of movement. A typical classification for the material properties distinguishes, for example, *"earth"* from *"debris"*, denoting as *"earth"* the materials with a maximum of 20% content of grains whose diameter is larger than 2 mm and using the term *"debris"* for the ones with a bigger percentage. It has, although, been shown that the limit of 20% for coarser grain has little significance in respect to the mechanical behaviour [8]. Therefore a characterisation by the material involved is more useful in a geological framework and for this reason it will be neglected here. For our purpose, the classification based on the sliding body motion mechanism is more interesting. Therefore Cruden & Varnes [4] distinguish five types of motion:

- **Slides**: are relative motions of the mass in respect to the stable material. Slides take place with velocity vector parallel to the sliding surface. The latter is a

clearly recognisable weakness region that separates the slide from the stable material of a slope. The movement can be either simultaneous for the whole slide or happen progressively. Slides can be divided further in:

  - *rotational slide*: the motion is roughly the rotation of the falling body about an axis that is parallel to the surface of rupture and transverse across the slide, Fig. 1.2A. In uniform materials the surface of rupture is upward concave spoon-shaped, but it may be different for geologic materials, where in general preexisting discontinuities influence the shape of the surface [19]. The movement velocity ranges from extremely slow to rapid, as the velocity is generally lower than 1 m/day;
  - *translational slide*: see Fig. 1.2B. Differently from rotational slides, the surface of rupture for translational slides is roughly planar. Depending on the dip angle of the surface of rupture, the slide can move extremely fast reaching values as high as 50 m/s and travelling for many kilometers; for this reason, a translational slide often stops beyond the surface of rupture. Fig. 1.2C represents a *block slide*, that is a particular translational slide where the moving mass can be a unit not greatly deformed or more closely related units moving coherently downslope;

- **Falls**: are abrupt movements of geologic material masses, i.e. rocks and boulders, that break away from steep slopes (Fig 1.2D). The movement occurs by free falls, bouncing and rolling where elevated velocities are involved;

- **Topples**: see Fig. 1.2E. Topples are distinguished by the forward rotation of one or more units around pivotal points. Triggers to the motion are forces exerted by adjacent units, water presence in cracks and, obviously, gravity. A topple is a tilting without collapse but, depending on the geometry of the detaching mass and on the orientation of the surface, it can evolve into a fall or a slide;

- **Flows** are the types of movement of unconsolidated material, that can be wet or dry. This motion is called *"flow"* because the distribution of velocities inside the moving mass resembles the ones observed within viscous fluids. Flows are distinguished in the following categories:

  - *debris flows*: are constituted by loose soil, rocks, organic matter, water and air that mobilise as a slurry flowing downslope, see Fig. 1.2F. The main cause of debris flows is an intense surface-water flow that takes place on steep slopes, due to heavy rainfalls or snowmelt. Debris flows are nearly saturated and consist of a large share of silt- and sand-sized material. They are always associated with steep gullies and move with velocities as high as 20 m/s [8]. For this reason they are characterised by high momentum

and high destructive potential. In fact debris flows tend to sort, bringing the largest clasts at the surface, where the flux velocity is higher. As a result the larger clasts travel faster and form the front of the debris flow. When debris flows move with extremely high velocity they are called *debris avalanches*. The latter have the peculiarity of being long and narrow (see Fig. 1.2G), leaving often a Λ-shaped scar on the slope. Vegetation on the slope has the property to diminish the susceptibility to debris flow;

- *earthflows*: are flows in fine-grained materials such as clay, silt and sand. They mostly take place on moderate slopes and under saturated conditions. However dry flows of granular material are also possible. In earthflows the slope materials liquefy and run downhill signing the slope with the characteristic "hourglass" shape represented in Fig 1.2H. When the material of an earthflow is wet enough to flow rapidly and contains at least 50% salt-, silt- and clay sized particles, it is called *mudflow*;
- *creep*: see Fig. 1.2I. Differently from the previous, creep is a steady and slow, nearly imperceptible motion of soil. Sources of motion are shear stresses not enough to cause failures but that, over long periods, deform permanently the material. Creep can be further divided in: (1)*seasonal*, where the deformation rate change with temperature and humidity; (2)*continuous*, where the shear stresses are steady in time; and (3)*progressive*, where at a certain point, the slopes reaches the point of failure. Typically creep is indicated by curved tree trunks, fences out of alignment and small soil ripples or ridges.

- **Lateral spreads**: see Fig. 1.2J. Usually spreads occurs on very gentle slopes or flat terrain where coherent material rests on incoherent one. The movement spreads laterally slowly (from 1 m/day to 0.1 m/min) and is accompanied by shear or tensile fractures. The failure is caused by a liquefaction process: sediments being saturated and cohesionless sands and silt, are transformed from solid to liquid state, diminishing their volumes. Failure is often triggered by an earthquake.

Generally, the motion of a landslide is more complex than the previous types that have been illustrated but can be seen as a combination of two or more of them. Therefore it is worthwhile to point out that a flow-like landslide is often the evolution of a slide [8].

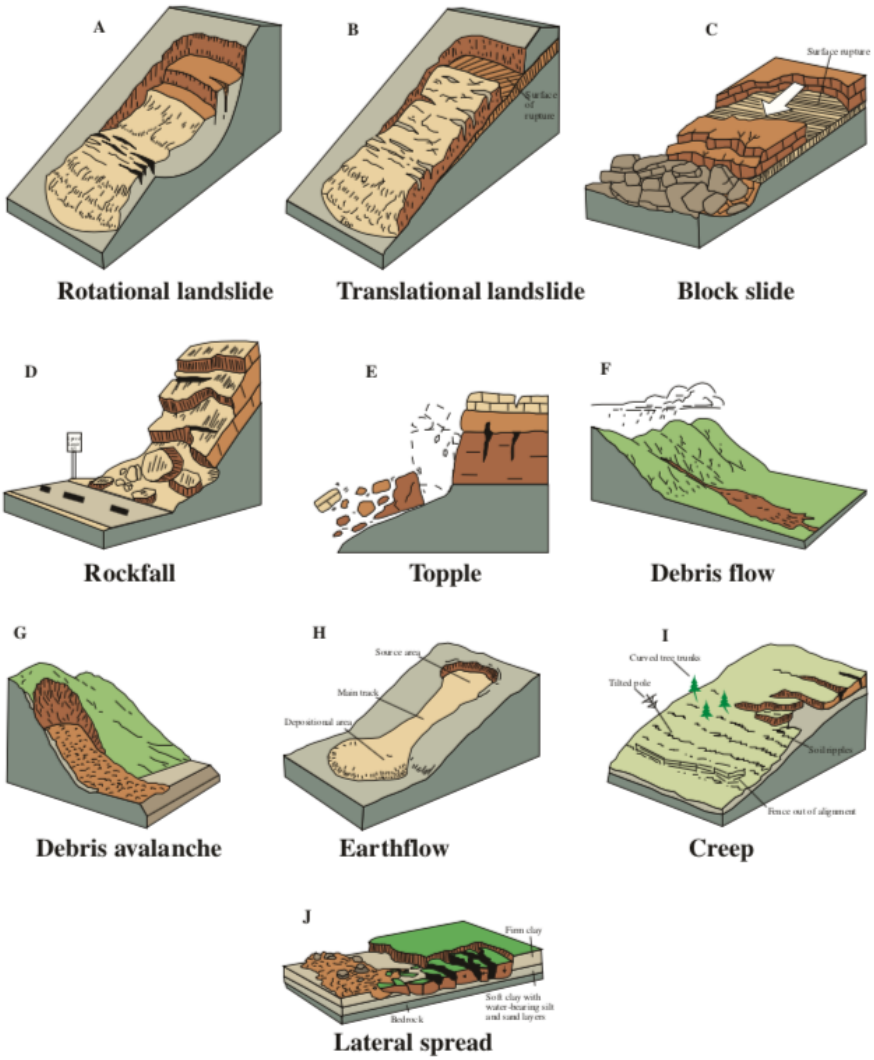

Figure 1.2: Major types of landslide movement. [Credit to USGS [18]]

1.3 Landslides causes

We will explain the Mohr-Coulomb failure criterion in order to understand what physically happens when a body becomes unstable. Let us start recalling that the maximum shear stress that a block on a surface can undergo without moving is expressed by the Amonton's law:

$$|\tau_{max}| = f_s p_n \tag{1.1}$$

where τ_{max} and p_n are respectively the maximum shear and pressure on the sliding surface. Amonton's law is the simplest way to model friction which is expressed by the friction coefficient f_s. Coulomb went further adding in the formula the cohesion coefficient c, i.e. a term that expresses how much rocks are welded together. Coulomb's formulation for the sliding criterion is:

$$|\tau_{max}| = f_s p_n + c \tag{1.2}$$

It is possible to express f_s as the tangent of the internal friction angle ϕ (later, the reason for this choice will be clear). To account for the water presence in the porous media, the normal stress p_n has to be corrected subtracting the pore pressure p_w. Let us call p'_n the difference $p_n - p_w$. Then the criterion that allows the motion is:

$$|\tau_{max}| = \tan(\phi) p'_n + c \tag{1.3}$$

Mohr's circle is a powerful representation for shear and normal stresses for every oriented plane of a body. If we limit our considerations to bi-dimensional problems (as planar stress or deformation configurations), in the main reference system the stress is a diagonal matrix with eigenvalues σ_1 (minimum), σ_2 and σ_3 (maximum). Consider a reference system rotated by an angle θ along the second main axis z. Stress tensor components, for this new reference system, are expressed as:

$$\begin{cases} \sigma'_{xy} = -R \sin 2\theta \\ \sigma'_{xx} = \bar{\sigma} + R \cos 2\theta \\ \sigma'_{yy} = \bar{\sigma} - R \cos 2\theta \end{cases} \tag{1.4}$$

where

$$\bar{\sigma} = \frac{\sigma_1 + \sigma_3}{2} \qquad R = \frac{\sigma_3 - \sigma_1}{2} \tag{1.5}$$

A visual representation of Coulomb criterion and Mohr's circle is shown in Fig. 1.3, where the shear and normal stresses are respectively on the y and x axis. Let us consider the line expressed by eq. 1.3 fixed in the plane and, varying values σ_1 and σ_3, notice the changes for circle's origin and radius. The failure takes place when the circle and the straight line are one tangent to the other. If this condition holds, the tangent point

coordinates are p'_n and τ_{max} and these stress values are the ones obtained rotating the main reference system by an angle θ_c. Looking at Fig. 1.3 it can be geometrically proven that $\theta_c = \frac{\pi}{4} + \frac{\phi}{2}$.

It is now possible to determine the factors that are the main slide causes:

- diminishing the minimum stress eigenvalue σ_1,
- increasing the maximum stress eigenvalue σ_3,
- diminishing the cohesion coefficient c,
- diminishing the friction angle ϕ;
- increasing the water table level.

Technically the landslide triggers are:

- lateral boundary removal,
- overloading of the surface of rupture,
- bottom support removal,
- lateral pressure,
- factor that diminish material resistance such as crushing and wet rocks

Combining Coulomb criterion and Mohr's representation with the trigonometric relation for θ_c, the Mohr-Coulomb criterion can be expressed as a relation for the stress eigenvalues:

$$\sigma_1 = \frac{1 + \sin\phi}{1 - \sin\phi}\sigma_3 + 2c\sqrt{\frac{1 + \sin\phi}{1 - \sin\phi}} \tag{1.6}$$

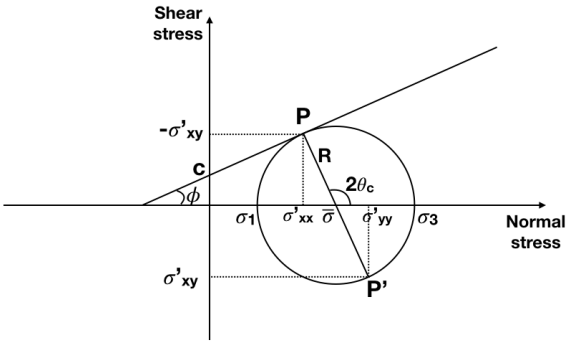

Figure 1.3: Mohr's circle: a generic stress state is described by the points P and P' on a circle of radius equal to the maximum shear stress and center on the abscissa axis on the medium normal stress $\bar{\sigma}$. The straight line represents Coulomb failure criterion.

1.4 Submarine landslides: a Tsunami source

The hazard related to submarine landslides have been underrated for long time. At the beginning they attracted the attention of researchers due to damages to submarine cables and to extraction platforms. But the awareness of their threat increased with time and nowadays it is clear that a submarine landslide can initiate violent waves that on reaching the coast can produce huge losses in terms of human lives and properties. Studying such events is the first step to mitigate terrible disasters such as the Aitape tsunami in Papua New Guinea (17th July, 1998) when a submarine landslide triggered by a Mw=7.0 earthquake caused a tsunami that attacked the cost of Aitape killing more than 2700 people.

In addition to mass collapses that undergo their motion completely underwater, also subaerial landslides that enter a basin can displace a large amount of water creating dangerous waves.

Submarine landslides are not too different from landslide events confined above the water surface. Their type of movement is classified in slides, flows and falls types. While falls are observed only in the proximity of very steep bathymetries, slides and flows can be found also where inclination angles are low. It is common that a submarine mass failure starts moving as a slide and then, due to the water presence and to fragmenting, its motion can evolve into a flow. Typical of submarine landslide motion is to evolve into a turbidity current [7], that is the term by which one denotes the motion of sediments under turbulent regime. Differently from subaerial landslides, submarine ones can travel for a very long distance (also called *run-out*) that can be as long as hundreds of kilometers. Moreover, collapsed masses are larger for submarine events and their volumes can reach thousands of cubic kilometers.

The regions where submarine collapses happen more frequently are characterised

by a marked steepness such as: seamounts and volcanoes' flanks, fjords, river deltas, submarine canyons and regions adjacent to the continental shelves. Large mass movements underwater displace large volumes of water creating perturbations in water free surface that propagate as waves. The latters transport and dissipate most of the kinetic energy released by the landslide.

The word *"tsunami"* is used to refer to the exceptional long waves that hit a shore. When the term was introduced, the focus was on the wave impact rather than on the source mechanism. In fact, the term comes from Japanese and its translation means *"harbour wave"*. Commonly, tsunamis follow submarine earthquakes due to normal or inverse faulting of the crust, but also landslides and volcanic eruptions can generate them. As regards Italy, in literature there are many examples of tsunamis associated to mass failures. It is worth to mention the Vajont reservoir disaster in 1963 [23] and the 1783 Scilla event [22].

Depending on the ratio of wavelength over water depth, water waves can be shallow, intermediate or deep. Basically, a shallow water wave is a perturbation of the water body whose length λ is several times larger than the water depth H (strictly speaking, the shallow water approximation is valid for $\lambda > 20H$). Differently, when $\lambda << H$, we are in the regime of deep water waves. Typically, tsunamis are shallow or intermediate water waves. Shallow water waves are not dispersive and can travel very far away from the source. On the contrary, deep water wave velocities depend upon the wave number k. For this reason, shapes of deep water waves spread during the propagation. Another aspect that depend on k, or equivalently on λ, is the energy dissipated by all types of the waves. The shorter the λ is, the faster the energy is dissipated. Therefore, deep water waves can become a threat only if the source of the perturbation is not too far from the shore hit by the wave. Although the impact of deep water waves is not dangerous far from the source, in the near field their arrival is obviously not enough delayed from the origin time, and this makes the deep water wave arrivals uneasy to forecast in time to prevent losses.

Shallow water (SW) waves can be a serious threat even if they are originated far from the shore since their energy is dissipated less during the motion. Far from the shore those waves are not elevated while their wavelength is huge. Because of this, the SW waves detection in deep water is rather difficult. These waves can travel very fast, in fact their phase velocity is equal to the square root of gH (where g and H are the gravitational acceleration and the water depth respectively). Approaching the shores, the velocity of SW waves decreases and, in order to conserve energy, the waves reach considerable heights. The impact on the shore can be devastating for the fact that most of the initial energy has not been dissipated during the motion and is released on the shore. To determine how impacting a wave on a shore can be it is useful to describe the wave in term of maximum elevation at the shore, also called *run-up*, of the distance traveled inland and of the velocity of the current developed in the flooded area.

Chapter 2

Vavilov seamount

2.1 Vavilov basin and seamount

The subject of this thesis regards scenarios of mass failure with tsunamigenic potential in the Vavilov seamount, a submarine mountain that was an active volcano in the recent past. The voluminous seamount (350-400 Km^3 [14]) lies at the center of the Vavilov basin which, in turn, represents the middle area of the Tyrrhenian Sea (Figs. 2.1 and 2.2).

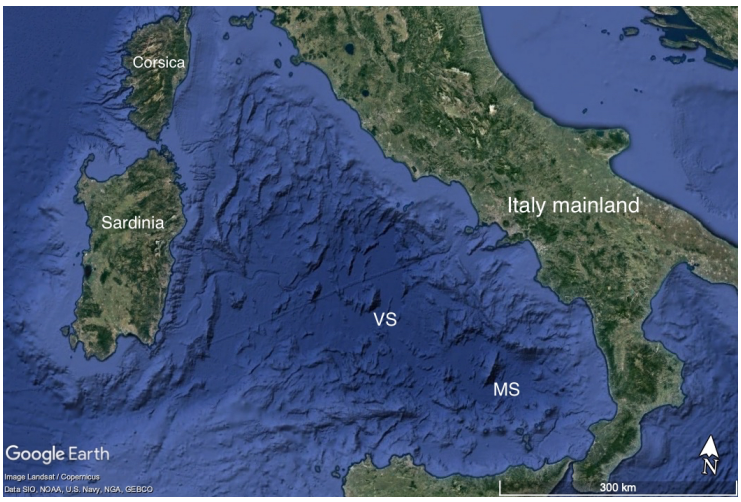

Figure 2.1: The Vavilov seamount (VS) is located in the middle of the Tyrrhenian Sea. The Marsili seamount (MS) is located 200 Km southeast of the VS. [Credit to Google Earth]

The Tyrrhenian Sea has a very complex geological history that has led to its present-day physiographic setting. It is an asymmetric basin that enlarges southwards. The

Tyrrhenian Sea is mainly characterised by extensional tectonics: the Ionian slab moves towards NW and subducts beneath the Tyrrhenian crust, where an extensional regime causes back-arc basin opening and volcanism [9]. Within the resulting geodynamic setting, the Aeolian islands are a typical volcanic arc and the Vavilov and Marsili volcanoes constitute the back-arc expansion zones. Hence the Vavilov and Marsili have similar genesis, yet they differ in age with the Vavilov being more ancient.

Savelli [16] recognises four phases in the evolution of the southern Tyrrhenian Sea. In the first phase, between 8 and 6 Ma (late Miocene), there was a strong acceleration in the rate of retreat of the Ionian subducting slab. In the meantime, a strong extension took place and brought the opening of the Vavilov basin, where basalts of MORB type (*Middle Ocean Ridge Basalt*) were erupted from the fissures. This aspect makes the Vavilov basin the oldest oceanic basin formed by back-arc extension in the Tyrrhenian Sea. In the second phase (between 5 and 2 Ma), during the Pliocene, the central Tyrrhenian zone which is occupied nowadays by Vavilov and Magnaghi seamounts, rifted and generated the two volcanoes. In the following phase (between 2 and 1.5 Ma), the extension zone moved southeast and brought to the Marsili basin's opening and the Aeolian arc volcanism. Finally, in the last phase (from 1.2 Ma to nowadays), the steepness of the subducting slab increased, its direction shifted from NW-SE to NNW-SSE and the Calabrian arc uplifted. Meanwhile the Aeolian arc and the Marsili seamount erupted volcanics with calcalkaline affinity while the Vavilov erupted volcanics with intraplate affinity that form its summit.

Differently from Savelli [16], Robin et al. [14] in a previous article, hypothesised that the Vavilov "does not represent a ridge related to the oceanic accretion as one might suppose". To sustain this thesis they recall that the base of the Vavilov is made of lavas strongly different from the underlying crust. Moreover, even if they agree on the two-phase generation of the volcano, they date Vavilov's deepest part to be not older than 2.4 Ma and the upper part to be 0.5-0.1 Ma old.

The Vavilov seamount's dimensions are reported by Gamberi et al. [6]: 33 km length, 17 km width and a relief of *ca.* 2700 m. Its axis slightly deviates from N-S trend, being oriented N10°. As a consequence, its flanks respectively face eastward and westward. A strong asymmetry between the flanks' slopes is a peculiarity of this seamount: the western side is steeper and smoother than the eastern one. Furthermore, the depth of the base of the two sides of the seamount is also different; in the eastern side the base is 3600 m below sea level (from now on *b.s.l.*) while, on the western side, it is at a depth of 3300 m.

For a description of the two Vavilov's flanks we refer to Robin et al. [14] that studied the seamount through underwater observations made on board of the "Cyana" submersible.

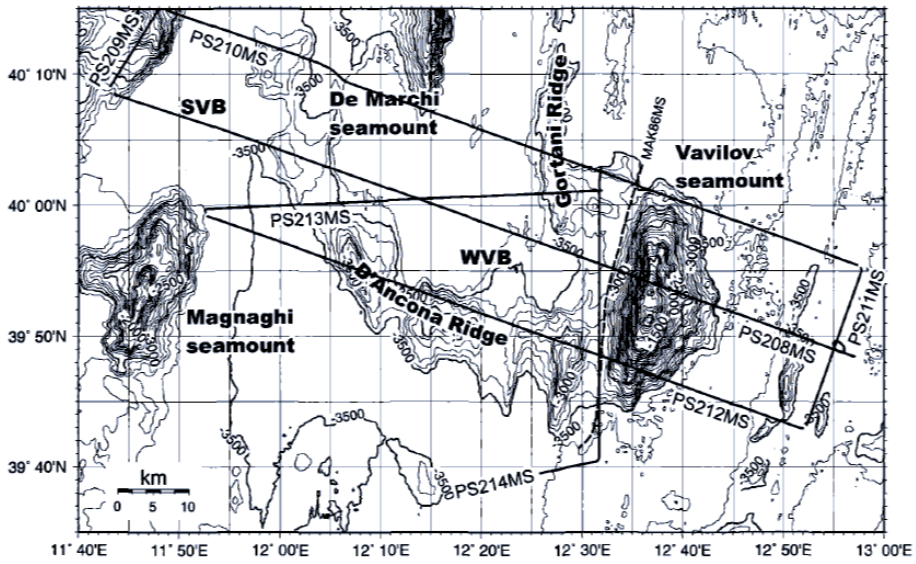

Figure 2.2: Location map of seismic lines in the Vavilov seamount region. Credit to Marani et al. [11]

2.1.1 The eastern side

The eastern flank of the seamount has a mean slope of 15°. From the ocean's bottom (-3600 m water depth) to 2000 m *b.s.l.*, the gradient rises progressively reaching values comprised between 5° and 10°. Then it further increases reaching 30° from 2000 to 1400 m of depth. Successively, the flank steepness diminishes becoming gentle up to 1000 m water depth. Finally, in the summit part (1000 - 864 m *b.s.l.*), the slopes become steep and smooth and their inclination angle is close to 35-40°.

It has been observed (*ibidem*) that the whole eastern flank is made up of volcanic material covered by a thin layer of sediments. Based on the morphology observed, Robin et al. [14] propose a division of the slope in three sections.

The lower part, from the basin plain to 1500 m deep, shows a stacking of successive basaltic flows with their edges mainly parallel to the seamount's elongation, i.e. N-S direction. All the flows observed in this part are fresh-looking bolsters or pillows with diameters ranging between 40 cm and 1 m. Small faults parallel to the seamount's axis were also observed.

The second section of the eastern flank goes from 1500 to 1000 m deep. It is characterized by a decrease in flows' thickness and a change in their source area being erupted by two upper volcanic centres. At 1010 m *b.s.l.* an abrupt depression with considerable dimensions (15 - 20 m deep) has been observed. It has been hypothesised

that it could be the edge of a caldera although more data would be needed to support this hypothesis.

The third, and last, section goes from 1000 m to the summit of the seamount (684 m *b.s.l.*). Here, the lava flows are radial and were emitted by a main vent forming a stratified cone whose summit does not show any crater.

2.1.2 The western side

The western side is smoother and steeper than the eastern one, in fact its dip mean value is 25°. The depth of the basin plain is 3300 m *b.s.l.*; remarkably, at 2990 m depth, a breccia composed of blocks and fragments of pillow lava was sampled under few decimetres of sediments [14]. Robin et al. *ibidem* explain the breccia as due to surface fragmentation of lava flows during cooling. It is interesting to point out that any breccia was not sampled on the eastern slope.

2.2 Hypothesis for the slopes asymmetry

The morphologic differences in the two flanks of the seamount have produced two different explanations and it is worthwhile to present both. As we reported in the previous paragraph the two flanks differ mainly for their mean steepness (the western mean slope being greater, 25° versus 15°), smoothness (the western flank being smoother) and for the different depths of the two sides of the basin (the eastern side being at least 100 to 300 m deeper than the western).

Robin et al. [14] suppose that, as the Sardinian block, the whole Vavilov basin tilted about its longitudinal axis toward west. They estimate the tilting angle to be of at least 10-15° and to support this thesis they recall the difference in the flank dip and the presence of normal faults parallel to the elongation of the seamount. On the other hand, Caratori et al. [3], on the basis of a theoretical original symmetry between the two flanks, hypothesised that the collapse of a mass of at least 50 km^3 from the western Vavilov flank is responsible for the observed asymmetry. In agreement with the collapse hypothesis, Marani & Gamberi [10] suppose to interpret the difference in sides depths as due to the accumulation of the material detached from the western flank.

Thus, the collapse scenario fulfils all the requirements of smoothness, inclination and depths asymmetry while the tilting hypothesis explains only the difference in inclination. However, tilting cannot altogether be excluded and could have contributed to seamount instability: a tilting would increase the angle for the western slope and consequently the probability of collapses.

It is more than worthwhile to note that the hypothesis of a past collapse, even if highly suggested, it is not fully substantiated by the few seismic profiles available over

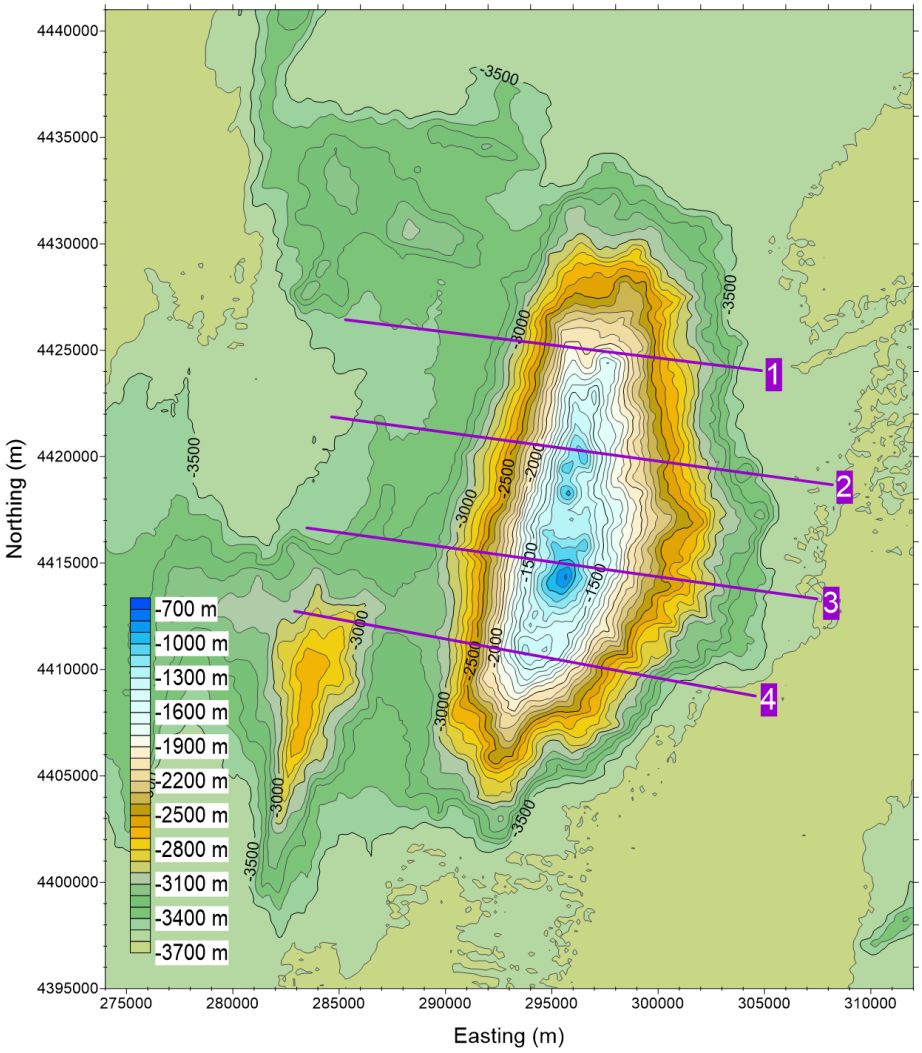

Figure 2.3: Current bathymetry of the Vavilov seamount. Coordinates are expressed in the WGS84 UTM33 reference system. Bathymetric data retrieved from EMODnet database [5]

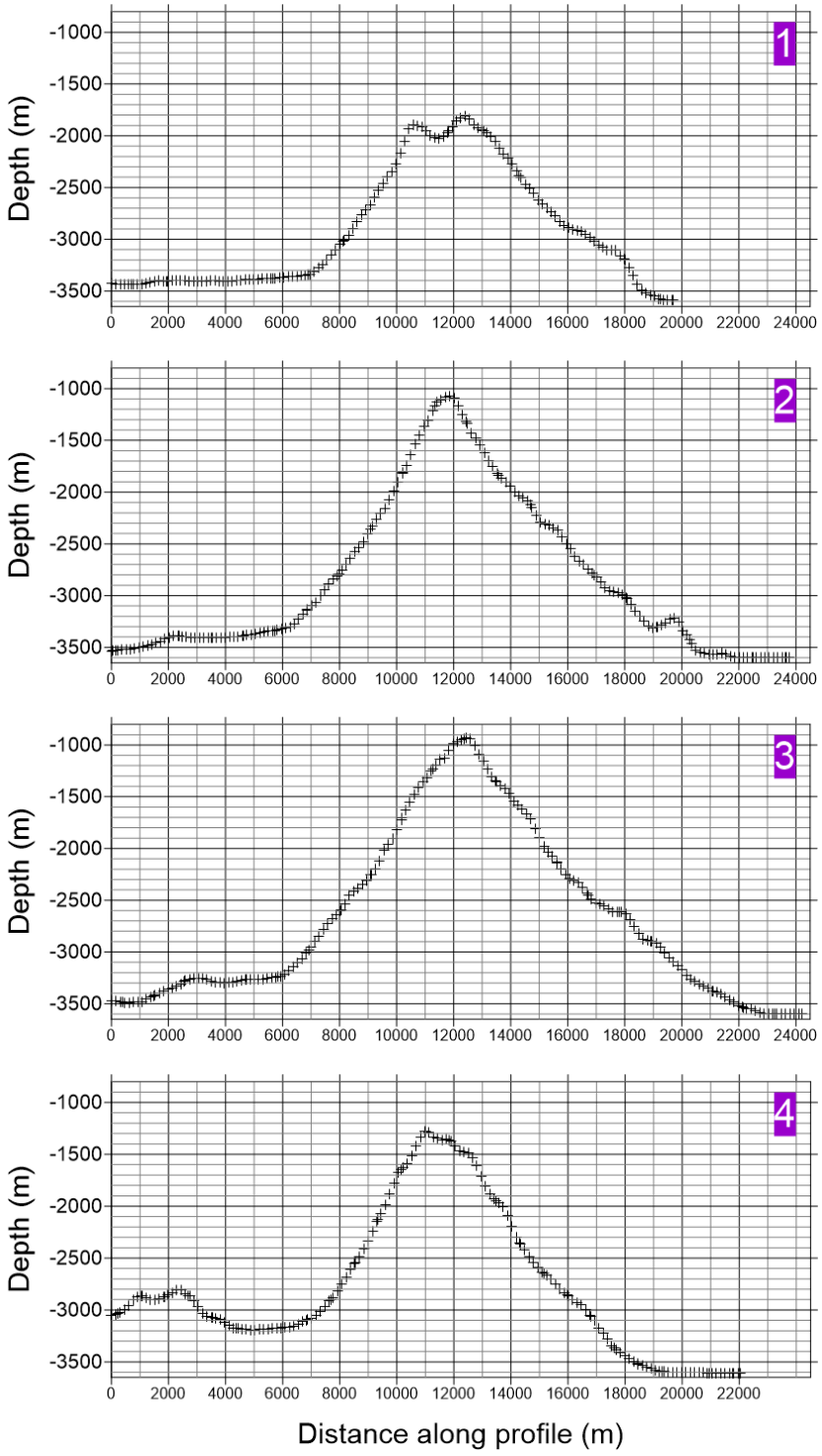

Figure 2.4: Profiles of the current bathymetry of the Vavilov seamount along the purple lines shown in Fig. 2.3

the study area (Fig. 2.2) that have been reproduced in Fig. 2.5. On the one hand, one can identify a region, located just to the feet of the of the seamount, where the regularly planar sedimentary cover that characterises the stratigraphy of the abyssal plane is disturbed by some irregularly accumulated rocky material that is compatible with the hypothesis of a collapse deposit. This is visible between 4 and 5 s Two-Way Travel Time (TTWT) in the seismic section of line PS208MS which crosses the Vavilov transversally, but also in the seismic section of line PS214MS that crosses the area facing the seamount longitudinally very close to it. On the other hand, the seismic profiles fail in showing clearly a body that can represent the result of the seamount failure. However, the deposit could have a seismic facies not distinguishable from that of the normal volcanic basement of the area. Moreover, a deposit would have been covered by sedimentation that is evident in the seismic profiles. Hence, if a collapse happened, it has to be a remote event.

In conclusion, even if the collapse has never occurred, yet our study has a great importance in showing the possible outcome of a failure of the Vavilov seamount that, given its steepness, is surely an area for which collapse can be expected. With this in mind, the estimated effects of the generated tsunami on the coasts can be used as guidelines for possible hazard scenario of realistic catastrophic events and to plan emergency operation in the coastal area.

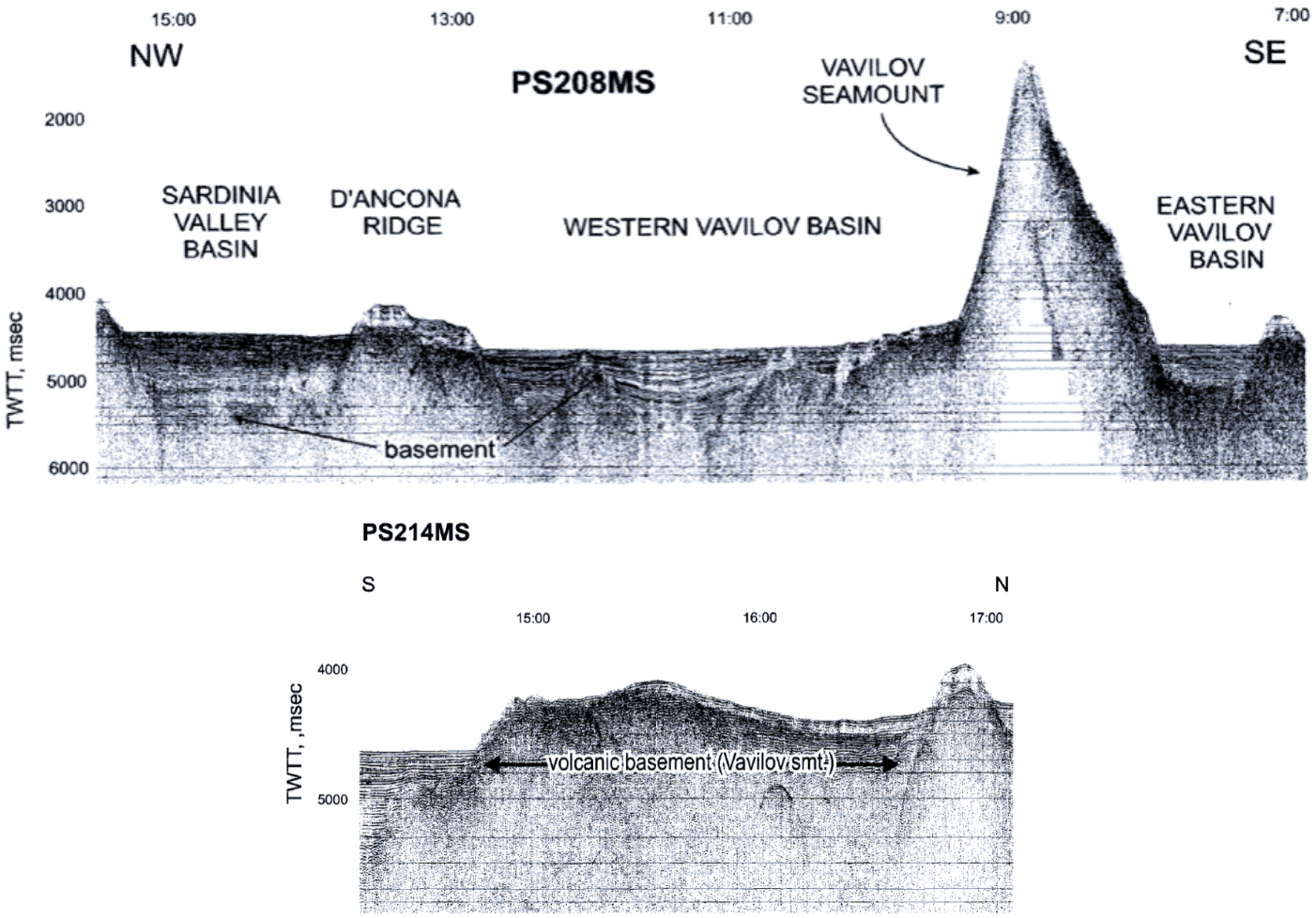

Figure 2.5: Seismic profiles over the lines PS208MS and PS214MS (shown in Fig. 2.2) in the Vavilov seamount region. [Credit to Marani et al. [11]]

Chapter 3

Physical models for a landslide

Introduction

The topic of this chapter is the modeling of a landslide. The first section is an overview of the physical assumptions that are generally adopted. This overview is important to collocate UBO-BLOCK2 in the variety of models that have been developed. In fact UBO-BLOCK2 is the model used for the simulation of the western flank collapse of the Vavilov seamount. A detailed description of how the bi-dimensional version UBO-BLOCK2 works will be presented in the second section.

3.1 Landslide models: a brief overview

As was discussed in Chapter 1, the motion of a landslide is complex since it is generally a mix of various types of motion. Moreover, it is difficult to determine the total collapsed mass and to identify the sliding surface. Therefore, modeling the landslide is a task that can be achieved only making some assumptions and, besides them, the equations obtained are not analytically resolvable but only numerically. Numerical models discretise both the space and time in order to avoid dealing with the continuum domain. Lagrangian models apply the governing equations to the spatial grid computing how it evolves at increasing time.

The first step to accomplish to model a landslide is to choose one of the two equivalent physical approaches, that are: following each single particle in its motion is the *"Lagrangian"* approach, while considering the flux properties at a given space position is the *"Eulerian"* approach. Depending on the approach used, the way derivatives are calculated changes. While the Lagrangian time derivate of a scalar quantity $T(\mathbf{x}, t)$ is defined as:

$$\frac{DT}{Dt} = \lim_{\Delta t \to 0} \frac{T(\mathbf{x}, t + \Delta t) - T(\mathbf{x}, t)}{\Delta t} \tag{3.1}$$

in the Eulerian approach it is:

$$\frac{DT}{Dt} = \lim_{\Delta t \to 0} \frac{T(\mathbf{x} + \mathbf{dx}, t + \Delta t) - T(\mathbf{x}, t)}{\Delta t} = \frac{\partial T}{\partial t} + \frac{\partial T}{\partial x_j}\frac{dx_j}{dt} = \frac{\partial T}{\partial t} + \mathbf{v} \cdot \nabla T \tag{3.2}$$

where summation convention is used (repetition of the same index j implies the summation over j). It is interesting to note that the term $\mathbf{v} \cdot \nabla T$, called *advection* term, becomes a quadratic term if we consider the total derivative of the velocity vector. This means that the Eulerian formulation of the Newton's second law is a non-linear differential equation for the velocity vector, making its analytical solution a hard task.

Besides the complexity of dealing with advective terms, Eulerian approach is usually preferred in Continuous mechanics because adopting the Lagrangian one is practically impossible when the number of particles is huge. Many models adopt the Eulerian approach because they consider the down-slope motion of a landslide as a flux of continuous and homogeneous material. This is one of the assumptions we had previously mentioned because a landslide is neither continuous nor homogeneous: in fact, it is a mixture of water, air and grain of different sizes that, by fragmenting, reduce their volumes. On the other hand, the continuum assumption has been proved to hold if the sizes of the grains are small compared to the depth and length of the landslide [15].

In modeling the tsunamigenic landslide behaviour, researchers have to deal with the coupling between the moving mass and the seawater. In fact, the interaction with water makes the landslide to change its shape and velocity. In turn, these changes modify how water is displaced during the mass motion. Some models neglect the coupling between mass and water and assume the landslide as a non-deformable piston that constitutes a time variable bottom boundary condition for the water. More sophisticated models deal with the coupling aspect treating the submarine motion as a problem of stratified fluid, where each layer is characterised by its own density and rheology.

Yavari-Ramshe & Ataie-Ashtiani [20] make a comprehensive review of the rheologies adopted to model a landslide. They propose a general form for the deviatoric part of the stress tensor expressed by:

$$\tau_{ij} = \tau_c + a e_{ij}^n + b(v) \tag{3.3}$$

where τ_c is a critical value for the shear stress τ, U is the flow velocity and the parameters a, b, n, τ_c for common rheologies are reported in table 3.1.

A material, such as the water, that cannot sustain shear stress without deforming is well described by the Newtonian rheology only if the strain rate is proportional to the applied shear stress. The proportionality constant is the viscosity μ. Differently, if the material shows a Newtonian behaviour only under shear stress greater than a critical value τ_c, then its behaviour is called plastic and Bingham rheology is the one that better represents it.

Table 3.1: Parametrisation of the rheologies commonly adopted in the models, as proposed by Yavari-Ramshe & Ataie-Ashtiani [20]. (c_z is the Chezy coefficient)

Rheology	τ_c	a	n	$b(U)$
Newtonian	0	2μ	1	0
Bingham	constant	2μ	1	0
Coulomb	$\sigma' \tan\phi$	0	0	0
Voellmy	$\sigma' \tan\phi$	0	0	$(U/c_z)^2$

While it has been proved by Pierson & Costa [13] and Abadie et al. [1] that landslides with less than 50% water content behave as viscoplastic fluids and above 50% resembles Newtonian fluids, those strain-rate-dependent rheologies are difficult to implement in a numerical model. Coulomb rheology appears to be simpler, in fact it assumes a constant value for the shear stress that is expressed in a friction-like formula. Voellmy rheology can be considered an intermediate choice between the Coulomb and Bingham rheologies because it introduces the flow velocity dependence for the shear stress. For this reason it is explained the widespread adoption of Coulomb and Voellmy rheologies in the models developed nowadays. In fact, the numerical solution of the equations yielded by the latter rheologies is easier than that yielded by other strain rate depending rheologies.

A completely different approach to model a landslide is the one used in the *"lumped"* models: these are models in which the landslide is divided in rigid blocks whose dynamics is determined considering the centres of mass of the blocks. An example of lumped model is UBO-BLOCK2 that approximates the landslide with a bi-dimensional matrix of blocks sliding on the surface of rupture. The blocks are able to deform providing a rough description of the shape of the landslide at evolving time. In addition their deformations account for the interaction with water, making the model able to simulate the motion of both submarine and subaerial landslides.

The approach adopted in the UBO-BLOCK2 model is clearly Lagrangian, being the centres of mass of the blocks the focus of the simulation. Although Savage & Hutter [15] adopted a Lagrangian approach too, their model differ from the UBO-BLOCK2 because Savage & Hutter consider the collapsed mass as a continuum with its own rheology. Instead, UBO-BLOCK2 model is more similar to Hutchinson's model that simplifies the whole mass considering it as a single sliding block [12]. The major limit of Hutchinson's assumption is that it cannot consider the changes in landslide's shape which, in turn, is a factor that surely affects the motion itself. On the contrary, UBO-BLOCK2 divides the landslide in many blocks and, allowing them to change shape but conserving volume, is able to account for their deformations.

3.2 Landslide numerical modeling: UBO-BLOCK2

UBO-BLOCK is a model developed by the University of Bologna Tsunami Research Team to simulate the landslide motion. The model consists in the discretisation of the landslide initial volume in a set of blocks that slide along a predefined surface. During sliding, mutual interaction between the blocks has, as a result, the deformation of the blocks themselves. Deformation of the blocks is limited by avoiding interpenetration. The dynamic of the center of mass is considered to model the motion of the whole block. The governing equation for each center of mass is the Newton's second law for a material point driven by gravity and affected by friction, drag and forces coming from the interaction with the other blocks.

It is important to stress out that the block division does not represent the fragmentation that occurs during a collapse, but it is rather a numerical expedient to account for the changes in shape of the mass. Moreover, although the model treats the landslide as a set of sliding blocks, it is not exclusively devoted to represent motions of the sliding type. In fact, the model computes centres of mass dynamical variables and the latters are not affected by the rheology of the mass. Hence, landslides that move as flows can be modelled by UBO-BLOCK as long as we are not interested in the velocity field within the flow.

The original model was developed by Tinti et al. [17] and consists in a 1D model that schematises the landslide in a chain of blocks. The developments of the 2D version are the results of the collaboration of the whole team and, in particular, of Bortolucci's [2] and Zaniboni's [21] efforts. The 2D model's advantage is to require as input data only the sliding surface and the pre-collapse bathymetry, hence it does not require the trajectories of the centres of mass as does the 1D model.

Basically, in UBO-BLOCK model the time is discretised by intervals Δt and for every time step, the dynamical variables of each block are computed. These variables at the i-th time step, for the k-th block are:

- position $\mathbf{x_{ik}}$, velocity $\mathbf{v_{ik}}$ and acceleration $\mathbf{a_{ik}}$ of the center of mass of the block;
- positions $\xi^{\mathbf{j}}_{\mathbf{ik}}$ and velocities $\mathbf{w^j_{ik}}$ of the vertices of the block (with j indexing the vertices);
- the time constant volume V_k of the block;
- the base area A_{ik} of the block;
- the height h_{ik} of the block.

3.2.1 Input data

The model UBO-BLOCK2 requires in input two surfaces: the first one is the sliding surface and the second one is the upper surface of the sliding mass before the collapse. Comparing the two surfaces, the code UBO-BLOCK2 computes the initial shape of the mass that will slide during the simulation.

The sliding surface

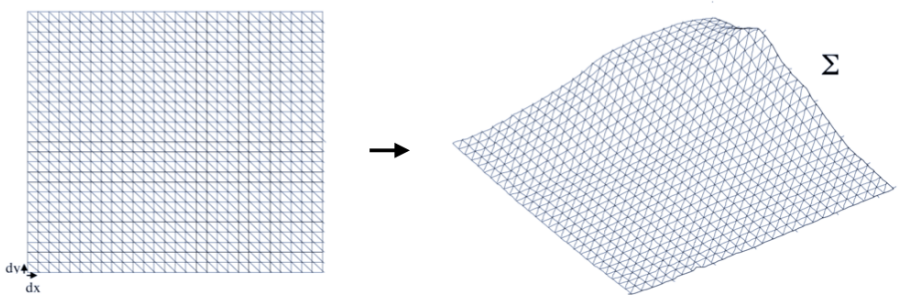

Figure 3.1: The regular domain (left) is projected on the sliding surface in order to obtain the numerical domain Σ(right) for the sliding surface. [Credit to Zaniboni[21]]

The sliding surface constitutes the domain over which the blocks move, but considering its real morphology is too computational expensive and depends on the available dataset. Hence, the sliding surface is approximated by a cover of triangles that are locally tangent to the surface. This operation is made by introducing a rectangular planar domain defined by the axis x and y (Fig. 3.1). The domain is discretised in intervals whose dimensions are respectively dx and dy. From this discretisation it is possible to originate a grid made of right triangles and to project them on the sliding surface. The cover of projected (not anymore right) triangles is the domain of the numerical simulation and it is called Σ. The smaller the dx and dy, the more accurate is the approximation.

Considered **dx** and **dy** the two unit vectors of the j-th right triangle, their projections over Σ are respectively the vectors $\mathbf{t_{jx}}$ and $\mathbf{t_{jy}}$. In order to define the latter projections, the components of the normal unit vector for the j-th triangle, $\hat{\mathbf{n}}_\mathbf{j}$ need to be defined. For this reason let us write the equation for the plane locally tangent to the sliding surface, that contains the j-th triangle of Σ as:

$$a_j x + b_j y + c_j z + d = 0 \tag{3.4}$$

It is now possible to compute the local unit vectors for the j-th triangle on Σ:

$$\hat{\mathbf{n}}_\mathbf{j} = \frac{1}{\sqrt{a_j^2 + b_j^2 + c_j^2}} \cdot (a_j, b_j, c_j) \tag{3.5}$$

$$\hat{\mathbf{t}}_\mathbf{jx} = \frac{1}{\sqrt{c_j^2 + a_j^2}} \cdot (c_j, 0, -a_j) \tag{3.6}$$

$$\hat{\mathbf{t}}_\mathbf{jy} = \frac{1}{\sqrt{c_j^2 + b_j^2}} \cdot (0, c_j, -b_j) \tag{3.7}$$

We are now able to express a generic vector $\mathbf{u}$ as a linear combination of the local unit vectors $\hat{\mathbf{t}}_\mathbf{jx}$, $\hat{\mathbf{t}}_\mathbf{jy}$, $\hat{\mathbf{n}}_\mathbf{j}$ as:

$$\mathbf{u} = u_{jx}\hat{\mathbf{t}}_\mathbf{jx} + u_{jy}\hat{\mathbf{t}}_\mathbf{jy} + u_{jn}\hat{\mathbf{n}}_\mathbf{j} \tag{3.8}$$

where the subscript j implies the local j-th triangle and thus stands for the components in the local reference system. Components u_{jx}, u_{jy}, u_{jn} can be calculated projecting $\mathbf{u}$ over the local unit vectors (that do not constitute an orthogonal base). After some calculations, we obtain:

$$\begin{cases} u_{jx} = \dfrac{(\mathbf{u} \cdot \hat{\mathbf{t}}_\mathbf{jx}) - (\mathbf{u} \cdot \hat{\mathbf{t}}_\mathbf{jy})(\hat{\mathbf{t}}_\mathbf{jx} \cdot \hat{\mathbf{t}}_\mathbf{jy})}{1 - (\hat{\mathbf{t}}_\mathbf{jx} \cdot \hat{\mathbf{t}}_\mathbf{jy})^2} \\ u_{jy} = \dfrac{(\mathbf{u} \cdot \hat{\mathbf{t}}_\mathbf{jy}) - (\mathbf{u} \cdot \hat{\mathbf{t}}_\mathbf{jx})(\hat{\mathbf{t}}_\mathbf{jx} \cdot \hat{\mathbf{t}}_\mathbf{jy})}{1 - (\hat{\mathbf{t}}_\mathbf{jx} \cdot \hat{\mathbf{t}}_\mathbf{jy})^2} \\ u_{jn} = \mathbf{u} \cdot \hat{\mathbf{n}}_\mathbf{j} \end{cases} \tag{3.9}$$

Thanks to these transformations it is possible to express every vector locally on the sliding surface Σ.

The sliding mass

To simulate the landslide, one requires to know the collapsing mass at the beginning time of the simulation. The collapsing mass is defined as the difference between the hypothesised pre-collapse bathymetry (undergoing the same triangulation procedure previously described) and the sliding surface. The user defines the number of blocks in which dividing the mass and has the option to choose between rectangular-base blocks (from now on called regular blocks) or irregular ones that are triangles or quadrilaterals, as shown in Fig 3.2.

For every block the code computes the base area at the beginning of the simulation, A_{0k} and the height h_{0k}. The volume V_k will remain constant for the whole simulation and it is computed by the simple multiplication $A_{0k} \cdot h_{0k}$.

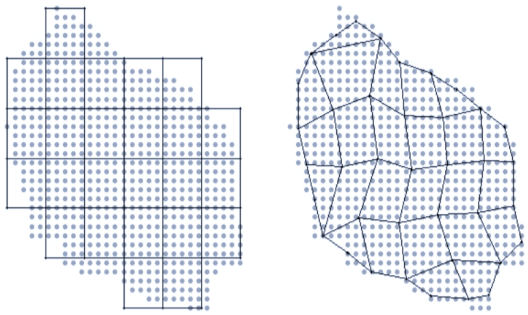

Figure 3.2: UBO-BLOCK2's subdivision of the collapsing mass into blocks. Blocks can be regular (right) or irregular (left). [Credit to Zaniboni [21]]

Although a regular subdivision does not reproduce precisely the borders of the landslide, it has the advantage of being handy for the numerical simulation and, for this reason it is generally adopted in the preliminary simulation. On the contrary, the irregular blocks subdivision constitutes a better approximation but suffers of some troubles during the routine execution. In fact, the model allows the blocks to deform and this feature can result in an unrealistic shape for those blocks whose geometries are greatly irregular at the beginning of the simulation.

3.2.2 The simulation

At time step i, the acceleration for the k-th block is the resultant of various terms:

$$\mathbf{a_{ik}} = \mathbf{G_{ik}} - \mathbf{R_{ik}} + \mathbf{F_{ik}} \tag{3.10}$$

where $\mathbf{G_{ik}}$, $\mathbf{R_{ik}}$ and $\mathbf{F_{ik}}$ are terms that respectively account for the gravity force, the drag forces exerted by the fluid where the block is immersed and for the interaction with the other blocks.

The motion can be expressed for its components in the local reference system. Hence, the eq. 3.10 becomes:

$$\begin{cases} a_{ik,x} = G_{ik,x} - R_{ik,x} + F_{ik,x} \\ a_{ik,y} = G_{ik,y} - R_{ik,y} + F_{ik,y} \end{cases} \tag{3.11}$$

while the acceleration in the $\hat{\mathbf{n}}_\mathbf{k}$ direction, that is the centripetal acceleration, can be derived from the position and the velocities of the block, since the motion takes place on the surface Σ.

The gravitative term

The gravitative term is the resultant of more aspects all related to gravity that are: the gravity component parallel to the sliding surface, the friction on the sliding surface and the buoyancy due to the medium in which the blocks are immersed. Thus the gravitative term is expressed as the vectorial sum of two terms that are respectively parallel and normal to Σ:

$$\mathbf{G_{ik}} = \bar{\mathbf{g}}^{/\!/}_{\mathbf{ik}} - \mu \cdot |\bar{\mathbf{g}}^{\perp}_{\mathbf{ik}}| \cdot \frac{\mathbf{v_{ik}}}{|\mathbf{v}_{ik}|} \tag{3.12}$$

where μ is the friction coefficient that governs the interaction between the block and the sliding surface. Applying the model to various real cases, the Tsunami Research Team has concluded that values of μ ranging between 0.15 and 0.25 and between 0.03 and 0.12 are appropriate respectively for the simulation of subaerial and submarine landslides.

As the reader may have noticed, eq. 3.12 is written for the k-th block which may occupy many, and perhaps also partially, Σ's triangles. Hence, the gravitative term is to be considered as a weighted average of all the contributes coming from the triangles spanned by the block, where the weights are the ratio of the occupied area. For a more detailed discussion we refer to Bortolucci [2].

In eq. 3.12 the bar over $\bar{\mathbf{g}}$ stands for the correction made to consider the buoyancy. In fact, a ρ density body immersed in a ρ' density fluid gets an up-toward pull equal to the load of displaced fluid. Thus, called $\bar{g}$ the resultant acceleration and considering a unitary volume, it holds:

$$\rho\bar{g} = \rho g - \rho' g \qquad \rightarrow \qquad \bar{g} = g\Big(1 - \frac{\rho'}{\rho}\Big) \tag{3.13}$$

If the landslide takes place in a subaerial set, the correction for the buoyancy is negligible while it is not for submarine events. It has to be pointed out that UBO-BLOCK2 is also able to deal with landslides whose dynamics takes place in both subaerial and submarine environment. In fact, eqs. 3.12 and 3.13 have been simplified in this dissertation, but their complete formulation that considers partially immersed blocks can be found in Zaniboni [21].

The resistive term

The resistive term for the k-th block is constituted by two main contributions, that are: the drag force exerted by the fluid on the top surface $\mathbf{R^{top}_{ik}}$ and on the exposed sides $\mathbf{R^{side}_{ik}}$:

$$\mathbf{R_{ik}} = \mathbf{R^{top}_{ik}} + \mathbf{R^{side}_{ik}} \tag{3.14}$$

The latter equation can be expressed for its components x and y as:

$$\begin{cases} R_{ik,x} = R_{ik,x}^{top} + R_{ik,x}^{side} \\ \\ R_{ik,y} = R_{ik,y}^{top} + R_{ik,y}^{side} \end{cases} \tag{3.15}$$

The drag force exerted on the top surface depends on the relative velocity between the block and the water. We consider the water resting, then the relative velocity is equal to the one of the center of mass. Thus, the components of $\mathbf{R_{ik}^{top}}$ are:

$$\begin{cases} R_{ik,x}^{top} = \dfrac{1}{2}\dfrac{\rho'}{\rho}\dfrac{C_d}{h_{ik}} u_{ik,x}\sqrt{u_{ik,x}^2 + u_{ik,y}^2} \\ \\ R_{ik,y}^{top} = \dfrac{1}{2}\dfrac{\rho'}{\rho}\dfrac{C_d}{h_{ik}} u_{ik,y}\sqrt{u_{ik,x}^2 + u_{ik,y}^2} \end{cases} \tag{3.16}$$

where C_d is the top drag coefficient and $\mathbf{u_{i,k}}$ is the velocity vector for the center of mass before accounting for the interaction term (the reason why $\mathbf{v_{i,k}}$ is not used here will be clear later).

The side drag term is the sum of the contributions coming from the four exposed sides of the considered block, as schematised in Fig. 3.3. Hence, neglecting for brevity the ik index, it holds:

$$\begin{cases} R_x^{side} = \sum_{j=1}^{4} R_{j,x}^{side} \\ \\ R_y^{side} = \sum_{j=1}^{4} R_{j,y}^{side} \end{cases} \tag{3.17}$$

The terms R_x^{side}, R_y^{side} depend on the angle α between the velocity vector's direction and the normal to the side j, and on the amount of exposed surface A_j^{exp}. Thus, the adopted formulas are:

$$\begin{cases} R_{j,x}^{side} = \dfrac{1}{2}\dfrac{\rho'}{\rho} C_f \dfrac{A_j^{exp}\cos\alpha_j}{V} u_{j,x}\sqrt{u_{j,x}^2 + u_{j,y}^2} \\ \\ R_{j,y}^{side} = \dfrac{1}{2}\dfrac{\rho'}{\rho} C_f \dfrac{A_j^{exp}\cos\alpha_j}{V} u_{j,y}\sqrt{u_{j,x}^2 + u_{j,y}^2} \end{cases} \qquad \cos\alpha_j > 0 \tag{3.18}$$

where C_f is the frontal drag coefficient while V is the volume of the considered block. The j-th contributions $R_{j,x}^{side}$, $R_{j,y}^{side}$ are computed by eq. 3.18 only if $\cos\alpha_j > 0$, i.e. only for sides that are facing the direction of motion. On the contrary, when $\cos\alpha_j \leq 0$, the side drag exerted on the j-th surface is neglected. For a detailed description of how the angle α_j is computed we refer to Zaniboni [21].

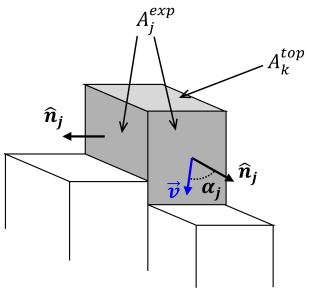

Figure 3.3: Scheme to compute the side drag exerted on the exposed side surfaces of a block. [Credit to Zaniboni [21]]

The mutual interaction term

The acceleration term due to the interaction acting on the k-th block is the sum of all the reciprocal interactions with the blocks that lay within an interaction range that will be discussed later. Called N the total number of the blocks, it holds:

$$\mathbf{F_{i,k}} = \sum_{j=1}^{N} \mathbf{F_{i,jk}} \tag{3.19}$$

UBO-BLOCK2 deals with a bidimensional problem, hence the interaction between the k-th and j-th blocks can have both the components normal and parallel to the direction of the centres of mass, resulting in forces for the blocks that can be both compressive/extensive and of shear type. Therefore, we break up the interaction $\mathbf{F_{i,jk}}$ into components respectively parallel to the direction connecting the two centres of mass $\hat{\mathbf{n}}_{\mathbf{jk}}^{/\!/}$, and perpendicular to the latter $\hat{\mathbf{n}}_{\mathbf{jk}}^{\perp}$ as shown in Fig. 3.4.

$$\mathbf{F_{i,jk}} = F_{i,jk}^{/\!/}\hat{\mathbf{n}}_{\mathbf{jk}}^{/\!/} + F_{i,jk}^{\perp}\hat{\mathbf{n}}_{\mathbf{jk}}^{\perp} \tag{3.20}$$

Similarly, the velocity of the centres of mass before the interaction $\mathbf{u_{ij}}$ and $\mathbf{u_{ik}}$ are expressed within the $\hat{\mathbf{n}}_{\mathbf{jk}}^{/\!/}$, $\hat{\mathbf{n}}_{\mathbf{jk}}^{\perp}$ base.

Hence, called M the total mass of the landslide and m_j the mass of the j-th block, the components of the interaction term come from the relations:

$$\begin{cases} F_{i,jk}^{/\!/} = C_{i,jk}\dfrac{m_j}{M\Delta t}\left(1 - e_{i,jk}^{1}\right)\left(u_{i,j}^{/\!/} - u_{i,k}^{/\!/}\right) \\ \\ F_{i,jk}^{\perp} = C_{i,jk}\dfrac{m_j}{M\Delta t}\left(1 - e_{i,jk}^{2}\right)\left(u_{i,j}^{\perp} - u_{i,k}^{\perp}\right) \end{cases} \tag{3.21}$$

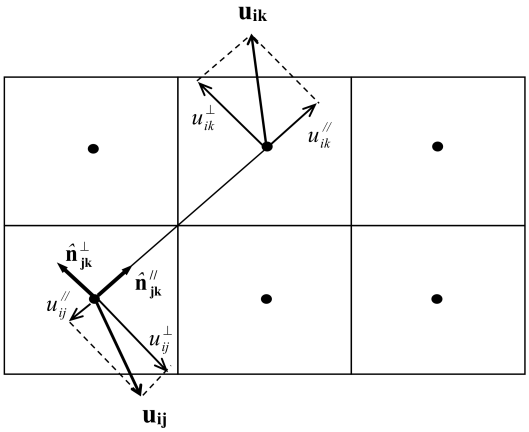

Figure 3.4: local reference system scheme adopted to compute the interaction term. [Credit to Zaniboni [21]]

where $e^r_{i,jk}$ is the interaction coefficient, that is calculated as:

$$e^r_{i,jk} = \begin{cases} f^r_{i,jk}\left(1 - \dfrac{\tau}{\sigma_r \delta t}\left|1 - \dfrac{|\Delta \mathbf{x_{i,jk}}|}{|\Delta \mathbf{x_{i-1,jk}}|}\right|\right)^{\gamma_r} & \text{if} \quad \Delta \mathbf{x_{i,jk}} \in I^r_{i-1,jk} \\ 0 & \text{if} \quad \Delta \mathbf{x_{i,jk}} \notin I^r_{i-1,jk} \end{cases} \tag{3.22}$$

with:

$$r = \begin{cases} 1 & \text{for the compressive/extensive case} \\ 2 & \text{for the shear case} \end{cases}$$

$I^r_{i-1,jk} \equiv \left[(1-\sigma_r)\,\Delta \mathbf{x_{i-1,jk}}; (1+\sigma_r)\,\Delta \mathbf{x_{i-1,jk}}\right]$ is the deformability range

$$f^r_{i,jk} = \begin{cases} 0 & \text{if} \quad \Delta A_{i,jk} \le (1-\sigma_{0,r})\Delta A_{0,jk} \\ \lambda_r\left[1 - \dfrac{1}{\sigma_{0,r}}\left(1 - \dfrac{\Delta A_{i,jk}}{\Delta A_{0,jk}}\right)\right] & \text{if} \quad (1-\sigma_{0,r})\Delta A_{0,jk} < \Delta A_{i,jk} < (1+\sigma_{0,r})\Delta A_{0,jk} \\ \lambda_r & \text{if} \quad \Delta A_{i,jk} \ge \Delta A_{0,jk} \end{cases}$$

$$\Delta \mathbf{x_{i,jk}} = \mathbf{x_{i,k}} - \mathbf{x_{i,j}}$$
$$\Delta A_{i,jk} = A_{i_j} - A_{i,k}$$
$$\Delta A_{0,jk} = A_{0_j} - A_{0,k}$$

Parameters adopted are:

- **interaction parameter** λ: is the maximum value for the interaction coefficient, λ ranges between 0 and 1, with $\lambda = 0$ the blocks are not allowed to deform and the whole slide moves as a single undeformable body. On the contrary, $\lambda = 1$ allows the blocks to the maximum interaction, hence to the maximum deformation;
- **deformability parameter** σ: accounts only for the deformation between the previous time step;
  - σ_0, that accounts for the deformation with respect to the beginning of the simulation;
- **shape parameter** γ: defines how the interaction coefficient e depends on $\mathbf{\Delta x_{i,jk}}$;
- $C_{i,jk}$ that governs the interaction range and assumes the values:

$$C_{i,jk} = \begin{cases} 1 & \text{if} \quad \mathbf{\Delta x_{i,jk}} < \mathbf{\Delta x_{min}} \\ \dfrac{|\mathbf{\Delta x_{max}} - \mathbf{\Delta x_{i,jk}}|}{|\mathbf{\Delta x_{max}} - \mathbf{\Delta x_{min}}|} & \text{if} \quad \mathbf{\Delta x_{min}} < \mathbf{\Delta x_{i,jk}} < \mathbf{\Delta x_{max}} \\ 0 & \text{if} \quad \mathbf{\Delta x_{i,jk}} > \mathbf{\Delta x_{max}} \end{cases}$$

  where $\mathbf{\Delta x_{min}}$ and $\mathbf{\Delta x_{max}}$ are user defined.

It is important to stress out that the resultant of the interaction between two blocks is always to reduce the differences in the velocities of the interacting centres of mass.

The time loop

To understand how the time loop works, let us consider the i-th time step: all the dynamical variables at the i-1-th time step are supposed to be known. It is not possible to numerically integrate eq. 3.10 in order to obtain the velocity because the interaction term depends on the velocity at the i-th time step. Therefore it should be clear why we define, for the time step i, two different velocities for the centres of mass, i.e. the one before the interaction $\mathbf{u_{i,k}}$ and the one after it $\mathbf{v_{i,k}}$.

The numerical integration is accomplished in two steps. Firstly, $\mathbf{u_{i,k}}$ is computed numerically integrating the acceleration at the previous time step (expressed by eq. 3.10) where we neglect the interaction term:

$$\mathbf{u_{i,k}} = \mathbf{v_{i-1,k}} + (\mathbf{G_{i-1,k}} - \mathbf{R_{i-1,k}})\Delta t \tag{3.23}$$

and, then we can deal with the interaction term with the computed $\mathbf{u_{i,k}}$. Hence, we update the velocities of the centres of mass through the numerical time integration of the interaction term:

$$\mathbf{v_{i,k}} = \mathbf{u_{i,k}} + \mathbf{F_{i-1,k}}\Delta t \tag{3.24}$$

The next step of the simulation is to determine the velocities $\mathbf{w}^{\mathbf{j}}_{\mathbf{i,k}}$ of the vertices of blocks: those are computed as a weighted average of the velocities of the centres of mass of its adjacent blocks. Knowing the velocities of the vertices, their positions are determined by a numerical integration. From the vertices positions $\mathbf{x}^{\mathbf{j}}_{\mathbf{i,k}}$ we can further compute the centres of mass positions, the areas $A_{i,k}$ and the heights of the blocks (by simply dividing the constant volumes V_k by A_k). After comparing the heights of the blocks, it is possible to calculate the exposed area of the sides. Then, for the i-th time step, all the dynamical variables are known and it is possible to repeat the calculation for the i+1-th time step.

The simulation is stopped in three different cases:

- one of the block is over-deformed by interaction with the other and its base is not anymore a quadrilateral or a triangle;
- the mass exits the domain Σ;
- the average centres of mass velocity is lower than a predefined value, meaning that the collapsed mass stops.

All the computations of the time loop are executed in the local curvilinear reference system. Therefore the variables need to be expressed in the cartesian reference system. For the transformations adopted we refer to Bortolucci [2].

Chapter 4

Results

4.1 Reconstruction of the Vavilov original morphology

In this thesis the main focus is the study of flank collapses of the Vavilov seamount. The assumption is that Vavilov suffered a huge collapse on the western flank and that this was responsible of the evident asymmetry of the seamount today's morphology. In order to simulate the mass failure, one has to reconstruct the original seamount shape before collapsing. To this purpose the following procedure was followed: removal of the east-west asymmetry in the bathymetry contour lines and restoring the original shape of the Vavilov's western flank by using the eastern one as a guide.

Two different hypotheses of pre-collapse flank have been explored. The first one, from now on called scenario 1, can be considered a preliminary work in which the western flank is reconstructed by adding to it the hypothesised collapsed material and the sliding surface coincides with the current bathymetry of the Vavilov seamount.

Differently, in the scenario 2, we observe that the region adjacent to the western flank is higher than the one adjacent to the eastern one, which could be a hint that originally the sea floor had the same depth on both sides of the seamount, and that the today difference is due to the accumulation of the the collapsed material on the western side. According to this view, in scenario 2, the assumed deposit is removed in order to uncover the surface on which the detached mass slides. The upper part of the sliding surface coincides with the one of scenario 1.

Workflow

Data from the online, open access EMODnet database [5] are used to draw a contour plot of the current bathymetry of the seamount and the surrounding region. The first step is data gridding: xyz coordinates points are transformed and converted in a grid 150x150 m expressed in the UTM coordinates system.

Then the sliding surface for the collapse is identified by using different strategies for the flanks, the crown and the toe of the surface of rupture. The flanks of the surface of rupture are delimited by those points where abrupt changes in contour lines may be recognised on moving across the contour lines along the side. The crown, i.e. the upper border of the surface of rupture, is chosen considering the contour line where one can find the highest bathymetric gradient close to the seamount summit. Indeed, the main scarp is characterised by its steepness. In scenario 1, as the toe of the surface of rupture we have basically chosen the contour line from which, going downslope, any change due to the collapse is not recognised in the bathymetry. A more rigorous procedure is followed for scenario 2: the deposit is identified making the western base as deep as the eastern one.

4.1.1 Scenario 1: the western flank before the collapse

Firstly, the surface of rupture is identified as illustrated by a magenta line in Fig.4.1. The area enclosed by the latter line is equal to 84 km^2.

Then, considering each single contour line inside the surface of rupture, the line itself is redrawn picking the points in a position that is further from the axis of the seamount. This operation is equivalent to add mass on the flank. Repeating the re-drawing for many contour lines inside the surface of rupture produces a dataset with xyz coordinates of the pre-collapse flank. This dataset is gridded and merged with the current bathymetry that have been previously blanked within the rupture area. In the overlapping regions (where the re-drawn contour lines follow the original ones), the mean value of the two grid is assumed in order to avoid discontinuities on the surface.

The result of the reshaping of the western flank for scenario 1 is shown in Fig. 4.2 and some corresponding cross-sections are given in Fig. 4.3. We notice that reshaping the western flank results in reducing the slope asymmetry between the two seamount flanks.

It is possible to estimate the collapsed mass volume by calculating the volume of the added mass. The latter is obtained by subtracting the current bathymetry elevation from the hypothesised pre-collapse one. This calculation yields a volume of 18.5 km^3 with a mean thickness of 220 m. The added mass thickness is shown with a colour scale in the contour plot of Fig. 4.2 where it has been superimposed to the Vavilov present bathymetry.

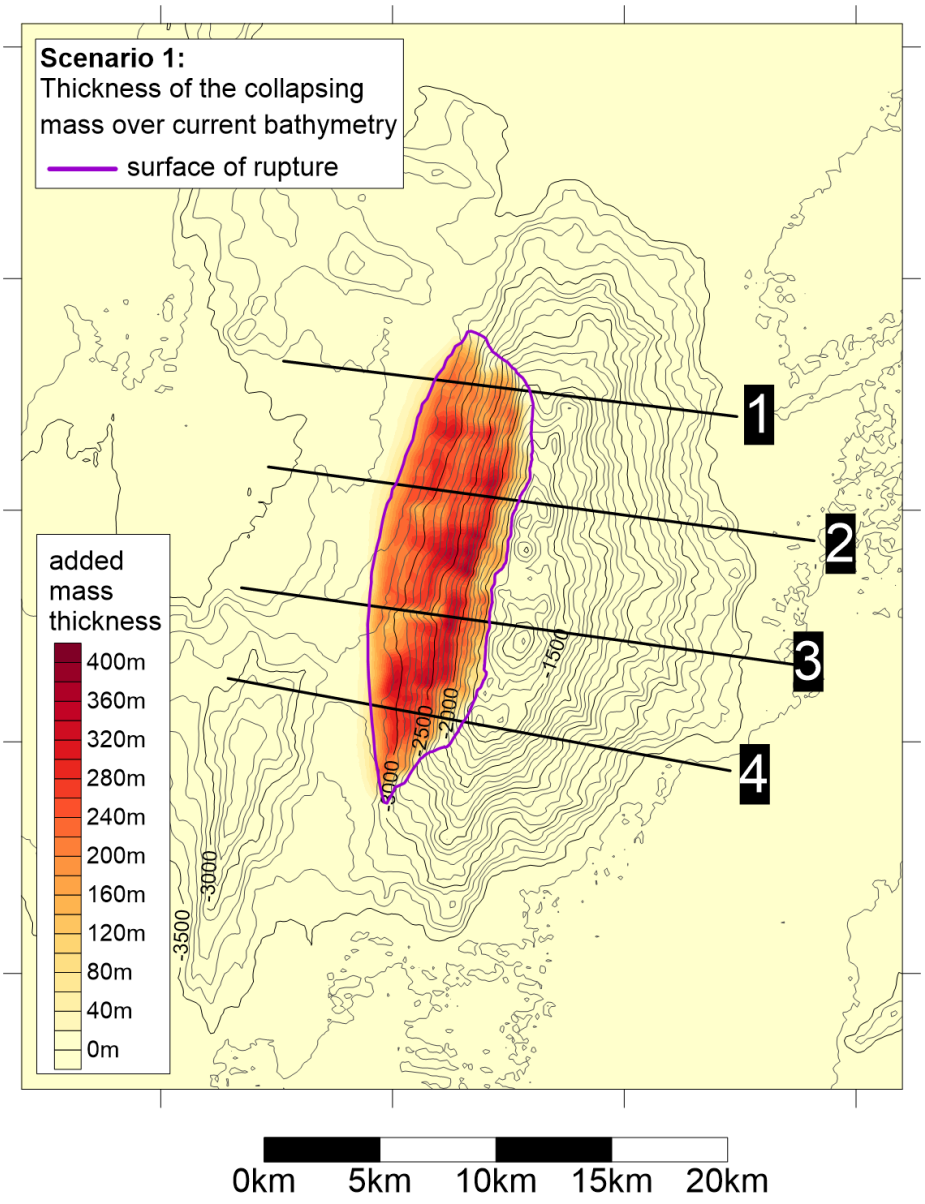

Figure 4.1: Scenario1: thickness of the added mass (colour scale) superimposed to the current bathymetry of the Vavilov seamount (lines). Magenta lines delimits the surface of rupture.

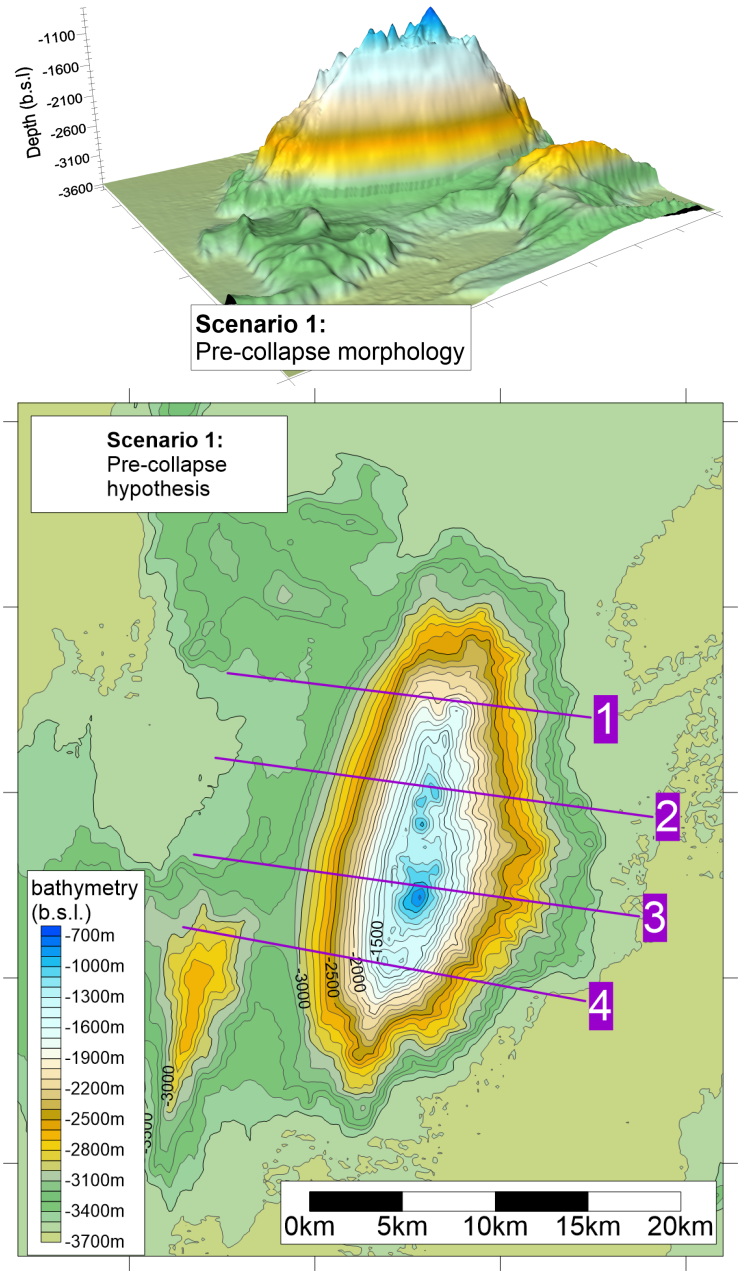

Figure 4.2: Scenario1: hypothesised pre-collapse bathymetry of the Vavilov seamount. Lines 1 - 4 are the ones used to generate the cross-sections of Fig. 4.3

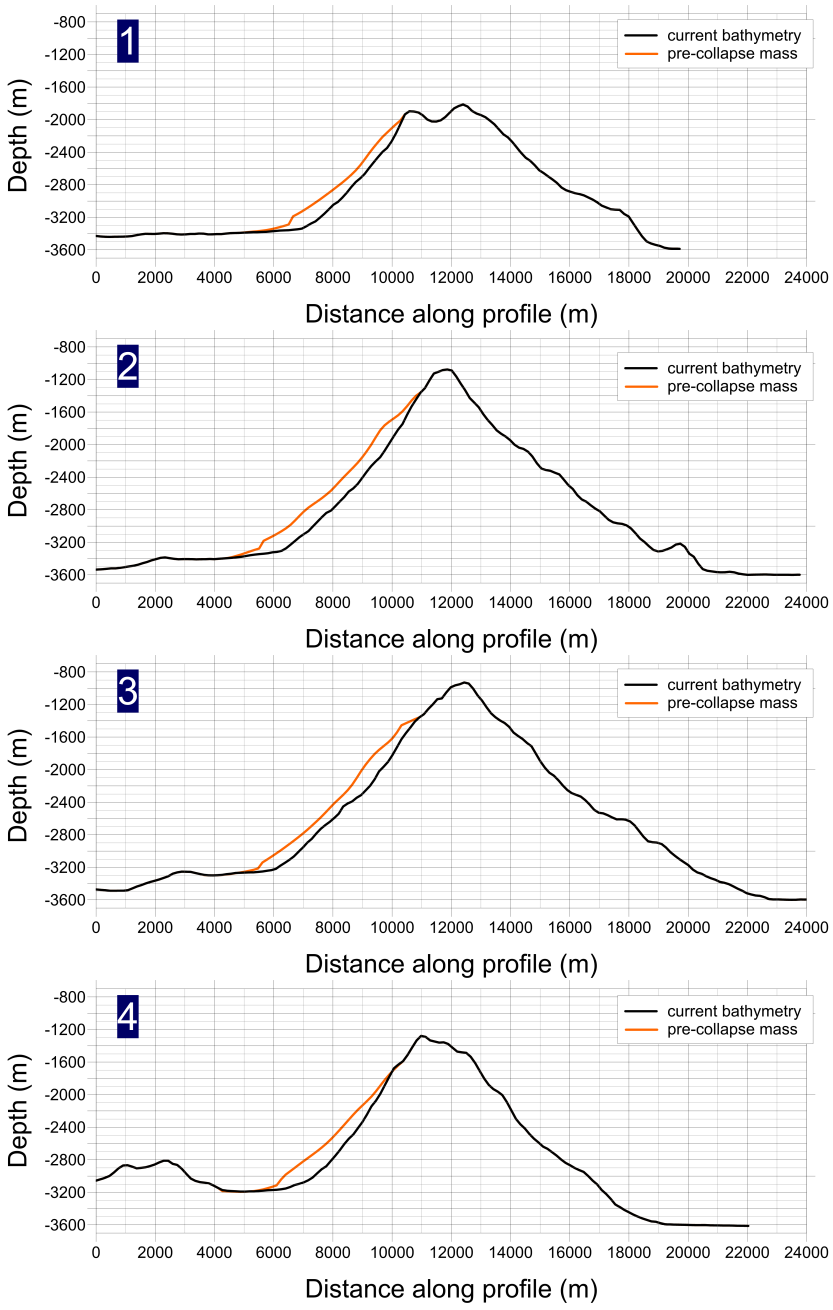

Figure 4.3: Scenario1: cross-sections of the current (black line), and pre-collapse (orange line) bathymetries along the four lines of Figs. 4.1 and 4.2.

4.1.2 Scenario 2: the western flank before the collapse

As discussed in section 2.1, the western Vavilov base lays at 3300 m *b.s.l.*, while the eastern one is roughly 300 m deeper. In scenario 2, the difference between the depth of the eastern and western plain is considered to be due to the deposit produced by the collapse of the western flank.

Hence, the contour lines in the region facing the western flank are redrawn in order to almost equalise the depth of the two bases. This operation is accomplished in a manner similar to the adding-mass-procedure followed for scenario 1: each contour line is redrawn but, this time, the new lines are drawn nearer to the seamount flank, lowering the basin plain. Then, gridding the generated dataset originates the morphology that constitutes the hypothesis for the sliding surface in this second scenario. The contour lines shown in the lower panel of Fig 4.4 are the result of the interpolation of the current bathymetry with the sliding surface (from now on called sliding bathymetry to simplify the notation).

The volume of the removed material is equal to 16.8 km^3 and its thickness is shown in Fig. 4.4. While in the northern part of the western basin the material was removed from a broad area, in the southern part the excavation area was limited by a sea bottom high. We have considered that this bathymetric feature existed before the collapse and therefore we have not removed it.

As for the scenario 1, the pre-collapse Vavilov western flank for scenario 2 was generated by adding mass to the sliding bathymetry in the region of the surface of rupture that is the same as scenario 1 (Fig 4.1). The pre-collapse hypothesised bathymetry is shown in Fig. 4.5. The added mass volume is equal to 17.5 km^3 and its mean thickness is equal to 210 m.

In Fig 4.6 one can see the cross-sections taken along the lines 1 - 4 pictured in Figs. 4.4 and 4.5. We can notice from the cross-sections 1 and 2 that the removal of material from the western basin plain makes the latter lying at the same depth of the eastern one for the northern zone (blue line). On the contrary, the material removed from the southern excavated region (cross-sections 3 and 4) lowers the sliding surface to the maximum depth of -3500 m, against the -3600 m of the northern zone. This difference is attributable to the necessity of connecting the sliding surface to the bathymetry of the sea bottom high.

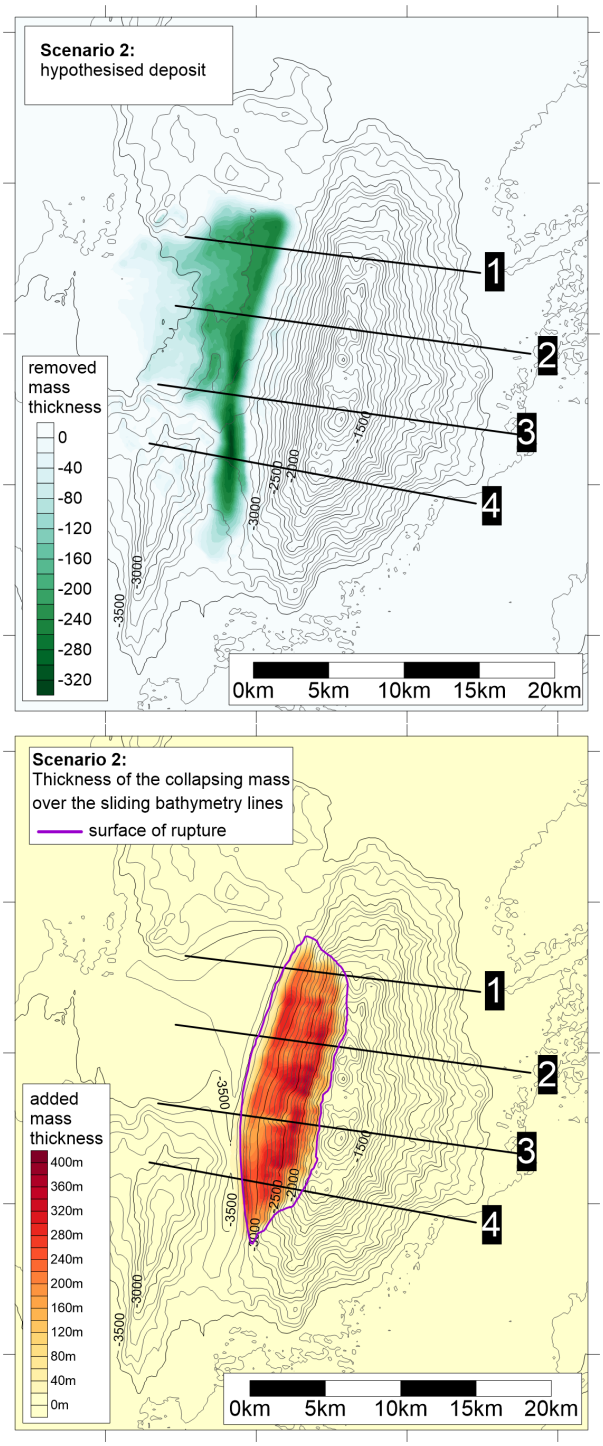

Figure 4.4: Scenario2: upper panel shows the thickness of the material removed from the current bathymetry. Lower panel shows the thickness added to the sliding bathymetry. The magenta line delimits the surface of rupture area and is the same of scenario 1.

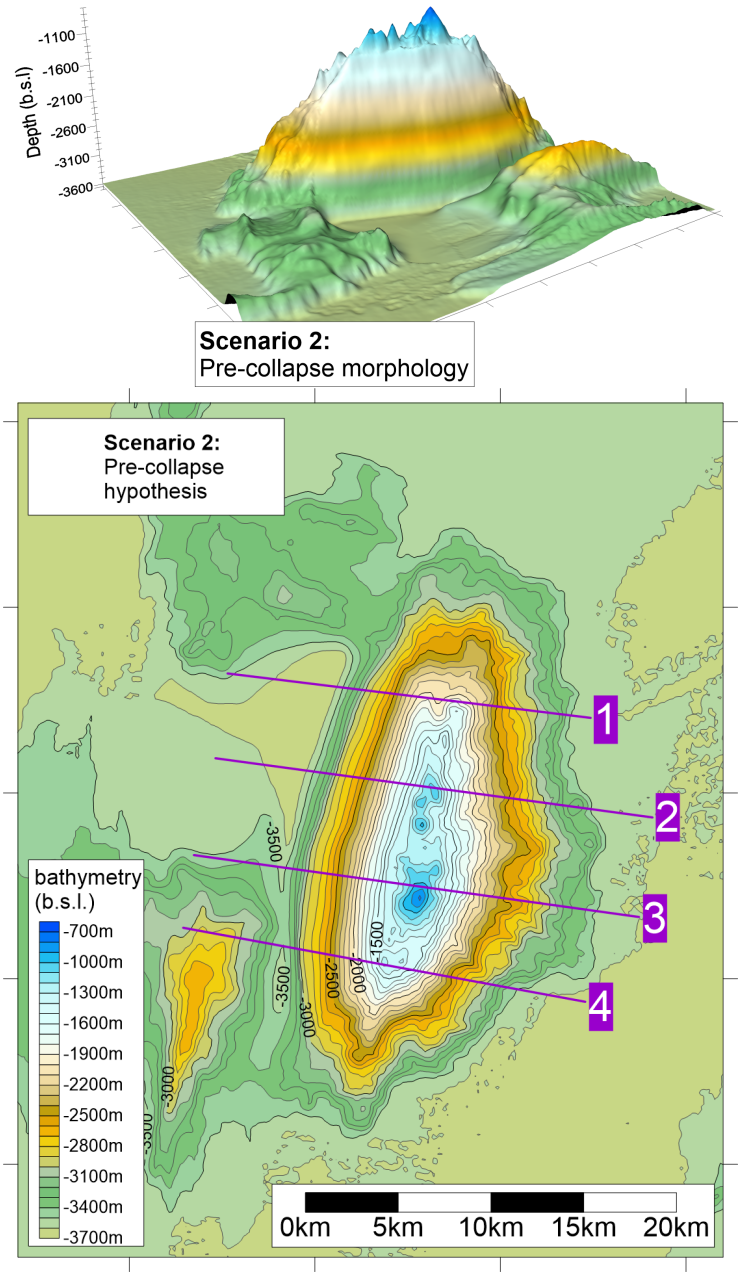

Figure 4.5: Scenario2: hypothesised pre collapse bathymetry of the Vavilov seamount.

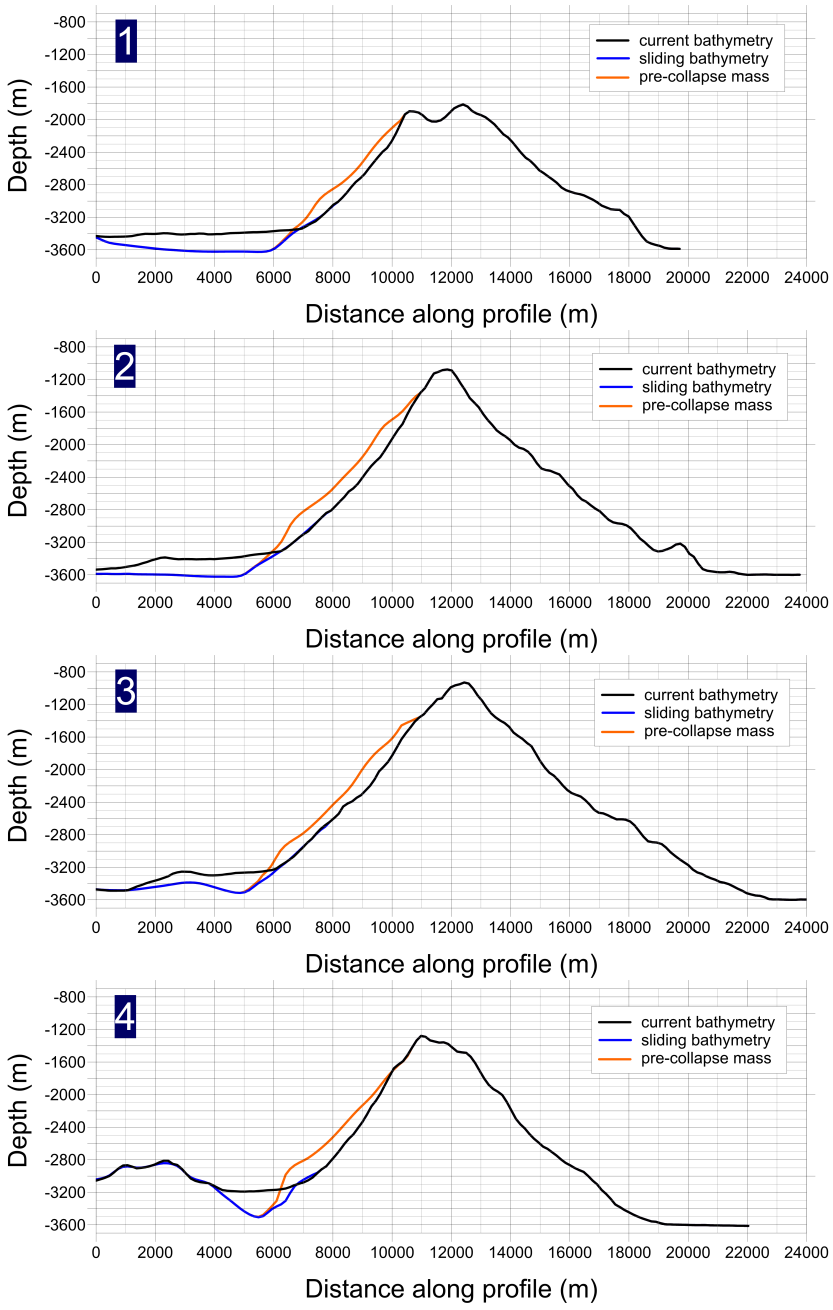

Figure 4.6: Scenario2: cross-sections of the current (black line), sliding (blue line) and pre-collapse (orange line) bathymetries along the four lines of Figs. 4.4 and 4.5.

4.2 Collapse simulations for scenario 1

In order to explore how the parameters of the model UBO-BLOCK2 affect the dynamics of the collapsing mass, the simulations for the Vavilov's scenario 1 have been carried out by changing the parameter's values within reasonable limits. The total number of runs for scenario 1 is 24. In the following we will identify the simulations by a number from 1 to 24, though not all of them will be illustrated. In this thesis, only the results needed to analyse the behaviour of the simulated blocks' dynamics under varying the grid type, the interaction coefficient λ, the drag coefficients C_d and C_f, and the friction coefficient μ will be reported.

4.2.1 Regular VS Irregular Blocks division

Simulations 18 and 15 differ only for the nature of the blocks in which the collapsing mass is discretised: for simulation 18 the mass is represented by a set of regular blocks, while they are irregular for simulation 15. In both simulations the number of blocks is equal to 26. The results are shown in Figs. 4.7 and 4.8.

It is interesting to note that the irregular block division properly approximates the collapsing mass at the beginning of the simulation. In fact, there is a good overlap of the block matrix with the surface of rupture that encloses the mass at the initial position. On the contrary, a regular block division yields a raw approximation.

Adopting an irregular block schematisation originates blocks that strongly differ as regards their base area. In particular the border blocks' shape is already greatly irregular at the beginning of the simulation. These blocks are the ones that will probably deform so much that their shape will lose any physical meaning. As discussed in section 3.2.1, in this situation UBO-BLOCK2 stops the simulation. This collateral effect has been noticed in several runs: in these cases the simulation has been conducted only for the regular blocks division.

The final stage of the simulation is evidenced in the two aforementioned figures by using a colour scale. The colours indicate the thickness of the calculated deposit. The block division scheme has been superimposed to it. The deposits for the two considered cases are very similar being practically equal in the central part where the majority of the mass is concentrated.

On the other hand, the shallow border area is broader for the simulation with the regular blocks. This aspect can be explained considering that the volume of the border blocks in the regular case is spanned over an area broader than the one for the analogous irregular blocks. Because of this, the height of a border block is lower in the regular case.

It is also interesting to notice that the southernmost block, that interferes with the sea bottom high, undergoes very different trajectories (black dots) in the two simula-

tions: in the regular case it climbs up the sea bottom high until a certain height and then slides back, while in the other case it reaches the top of the high and does not revert its motion. This aspect can be explained by the fact that the regular block is more extended southwards where the slope of the topographic high is more elevated, therefore it is subjected to a greater deceleration due to gravity.

The time series of the velocity module of the centres of mass of the blocks is shown in the lower panels of Fig. 4.9 for the regular and irregular blocks case. While the peak velocity is slightly higher for the regular blocks case, namely 52 m/s against 50 m/s, it is reached in the same time (t = 64 s). Even the duration of the slide motion is roughly equal to 275 s. Besides, in the regular case there are two blocks that, during the simulation, stop and start sliding again while this happens only for one block in the irregular case. This consideration is in agreement with what was said before about the southernmost block's dynamic.

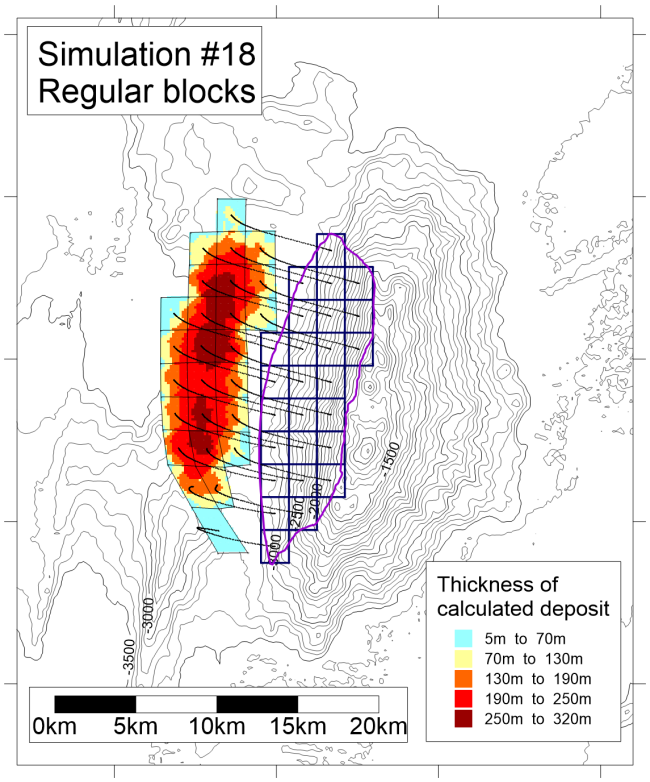

Figure 4.7: Blocks division of the collapsing mass. The mass is divided in 26 blocks (blue lines) that can be regular (Sim. 18) or irregular (Sim. 15, in the next figure). The simulated deposit thickness is represented in colours with superimposed the blocks structure at the end of the simulation (black line). The magenta line delimits the surface of rupture. The black dots represent the centres of mass of the blocks at evolving time steps.

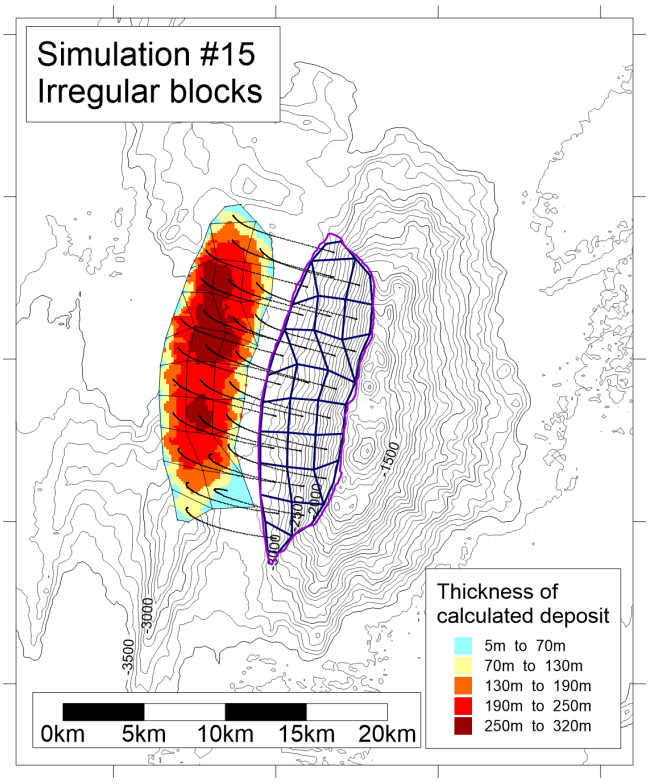

Figure 4.8: see caption of Fig.4.7

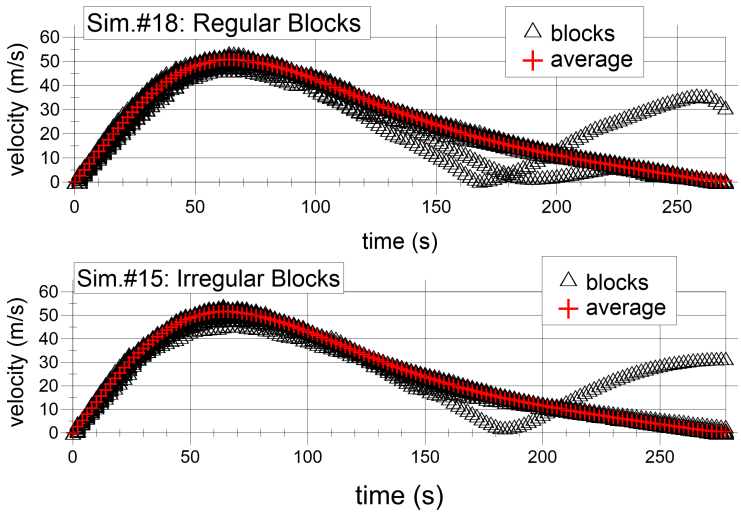

Figure 4.9: Velocities of the centres of mass of the blocks (triangles) and weighted average values (crosses) for regular (Sim. 18) and irregular blocks (Sim. 15).

4.2.2 Increasing the number of blocks

Simulation 21 was conducted with the same parameters of simulation 15, but increasing the number of blocks (98) that represent the mass. The upper panel of Fig. 4.10 yields that, with a greater number of blocks, the overlap between the initial blocks grid (black) and the surface of rupture is better approximated than in the case of 26 regular blocks. We further notice that the thickness of the simulated deposit is more detailed than in the both regular and irregular 26 blocks. The lower panel of Fig. 4.10 yields practically no differences with the previous cases with fewer blocks. In fact, the peak velocity is still reached at t = 64 s and its value (namely 50 m/s) is in agreement with the previous simulations.

It has to be pointed out that the time needed to model the sliding increases with the number of blocks.

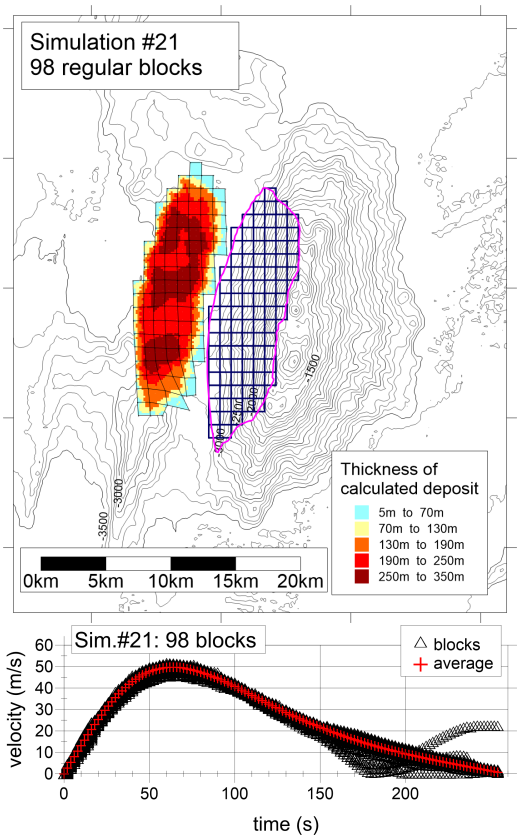

Figure 4.10: Blocks division of the collapsing mass, Sim. 21. The mass is divided in 98 regular blocks (blue grid). The simulated deposit thickness is represented in colours with superimposed the blocks structure at the end of the simulation (black line). The magenta line delimits the surface of rupture.

4.2.3 Tuning the interaction parameter λ

As discussed in section 3.2.2 the model UBO-BLOCK2 considers the mutual interaction between the blocks as an acceleration term that is expressed in eqs. 3.21. These formulas (and the ones following) depend on several parameters. Among them the parameter λ governs how the blocks can deform for effect of the interaction. In fact, $\lambda = 0$ is equivalent to consider an elastic interaction of the blocks, while setting $\lambda = 1$ means allowing the interaction to be inelastic.

Simulations 4, 20, 19 and 18 differ only for the interaction parameter value, being λ respectively equal to 0.5, 0.9, 0.95, 1. Hereafter we will show only the simulations in which the mass is divided in regular blocks because, in this way, it is easier to see how λ influences the deformation of the blocks.

For $\lambda = 0.5$ the final schematisation of the blocks (black grid of upper panel of Fig. 4.11) is practically the translation of the initial one (blue grid), meaning that the blocks do not deform during sliding. For higher values, such as $\lambda = 0.9$, a deformation is visible for the southern blocks. This deformation increases with $\lambda = 0.95$ (Fig. 4.12) and even more with $\lambda = 1$ (Fig. 4.7).

Figs. 4.13 and 4.9 (lower panel) portray respectively the modules of the velocities of the centres of mass for simulations 4, 20, 19 and 18, conducted for increasing values of λ. Varying the interaction parameter does not affect the maximum velocity reached nor the duration of the slide process. On the other hand, increasing λ allows some of the blocks (that we already depicted as the southern ones) to slow down on the topographic high and to behave differently from the rest of the slide. On the contrary, for low λ values all the blocks velocities do not differ from the average value. Meaning that there is a sort of pull exerted on the southern blocks by the others.

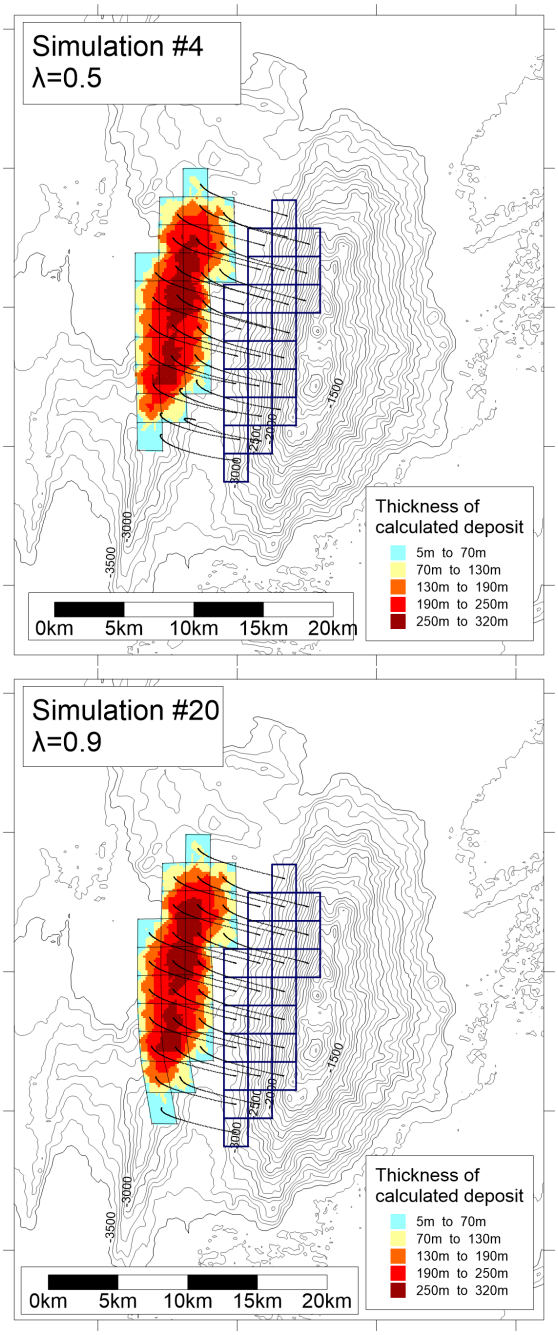

Figure 4.11: Results for values of λ= 0.5 (upper panel), 0.9 (lower panel) and 0.95 (in the next figure). The simulated deposit thickness is represented in colours with superimposed the blocks structure at the end of the simulation (black line). The black dots represent the centres of mass of the blocks at evolving time steps. The blue grid represents the blocks at the initial time.

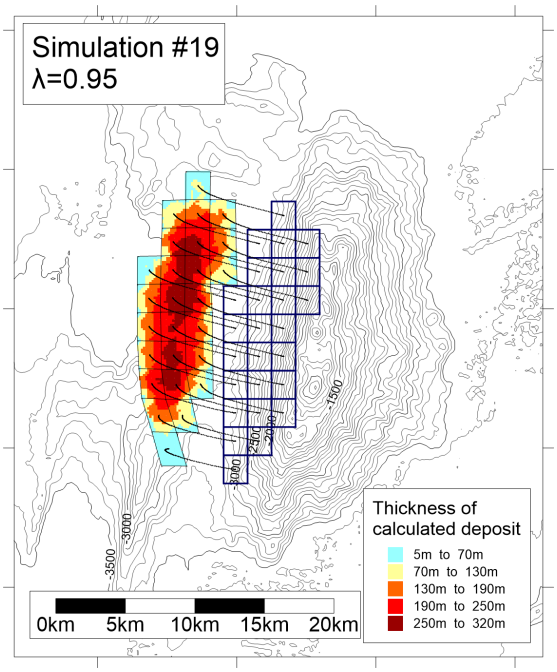

Figure 4.12: see caption of Fig. 4.11

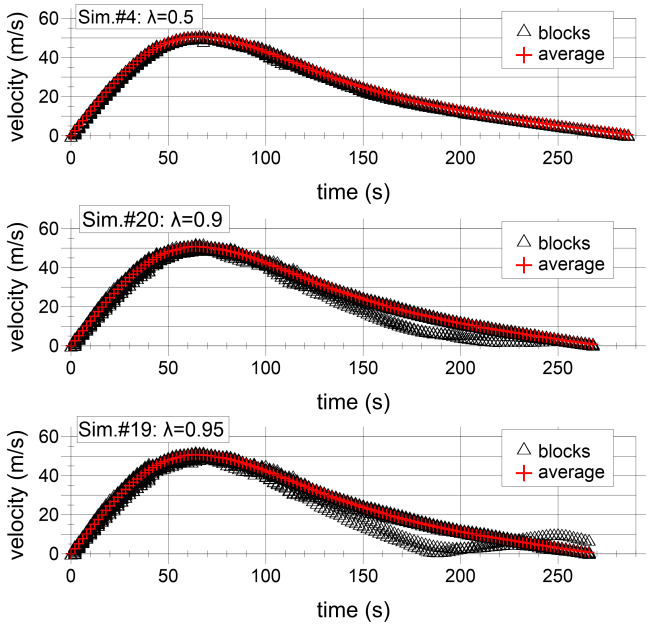

Figure 4.13: Velocities of the centres of mass of the blocks (triangles) and weighted average values (crosses) for simulations with λ equal to 0.5 (Sim. 4), 0.9 (Sim. 20) and 0.95 (Sim. 19).

4.2.4 Tuning the friction coefficient μ

The effect of varying the seafloor friction coefficient μ will be illustrated through the simulations 12, 15, 14 and 8 in which μ has been set respectively equal to 0.03, 0.06, 0.10 and 0.12. While the results of simulations 12, 14 and 8 are shown in Figs. 4.14-4.16, for simulation 15 we will refer to Figs. 4.8 and 4.9.

It is clear from these figures that varying μ does not affect the final thickness distribution of the calculated deposit. On the contrary, the run-out is strongly affected by the friction parameter. In fact, as expected, the lower is μ the farther the mass travels: for $\mu = 0.03$ the run-out is approximately equal to 12 km, while for $\mu = 0.06$, 0.10 and 0.12 the slide travels a distance that is respectively equal to 6400 m, 4800 m and 4200 m. Analogously, considering the velocity graphs one can note that for low values of the friction coefficient the time duration of the motion is higher. In fact, while the simulation for $\mu = 0.12$ lasts 172 s, the one with $\mu = 0.03$ lasts 578 s.

An important aspect governed by the friction coefficient is the value of the maximum velocity reached by the blocks during sliding. Considering the average value of this quantity one notes that the maximum velocity diminishes for increasing μ: the peak velocity is almost equal to 57, 52, 45 and 43 m/s for the increasing values of μ considered here. On the other hand, the time at which the maximum velocity is reached is roughly equal to 64 s for all the considered simulations. Hence, μ does not affect this feature of the motion.

We observe further that the velocity has a similar time evolution in all the simulations. Therefore we will refer to the velocity plot relative to simulation 15 (lower panel of Fig.4.9). Considering the time series of the average velocity as a continuous function, we propose to divide the motion of the blocks in three phases distinguished by the slope of the average velocity, i.e. the time derivate of the the velocity. The first phase is the one in which the average velocity increases linearly with time (from 0 to 25 s). Then, in the second phase, the slope of the velocity module decreases until being equal to zero in correspondence with the maximum velocity value (reached at t = 64 s). In the third phase the slope of the velocity is negative (from 120 s to the end of simulation).

By increasing μ, we observe higher differences in the third phase in which the motion has been divided. In fact, for all the simulations, the change of the slope that separates the first phase from the second one is seen at t = 25 s and the maximum is reached at t = 64 s. On the contrary, in the third phase, we notice that the time series of the average velocity is upward concave for $\mu = 0.03$ and $\mu = 0.06$, while for $\mu = 0.10$ and $\mu = 0.12$ it seems to have a linear time dependence. However, it has to be remarked that the short duration of the motion for simulations with higher μ makes it a difficult task to distinguish a slightly upward concave evolution from a linear time evolution.

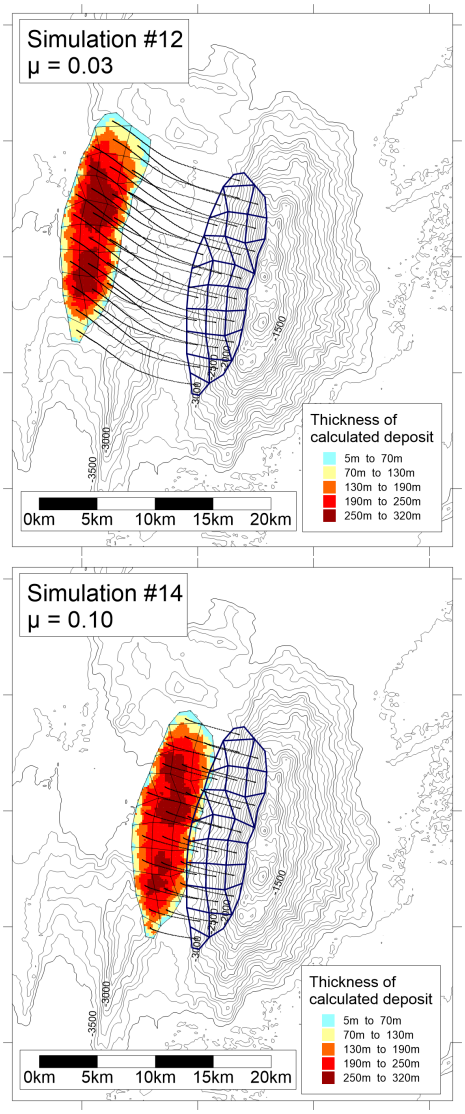

Figure 4.14: Results for runs with friction coefficient $\mu = 0.03$ (Sim. 12, upper panel), 0.10 (Sim. 14, lower panel) and 0.12 (Sim. 8 in the next figure). The simulated deposit thickness is represented in colours with superimposed block structure at the end of the simulation (black line). The black dots represent the centres of mass of the blocks at evolving time steps. The blue grid represents the blocks at the initial time.

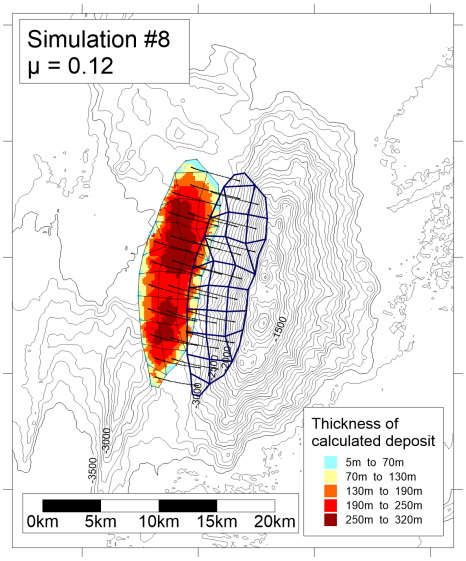

Figure 4.15: see caption of Fig. 4.14

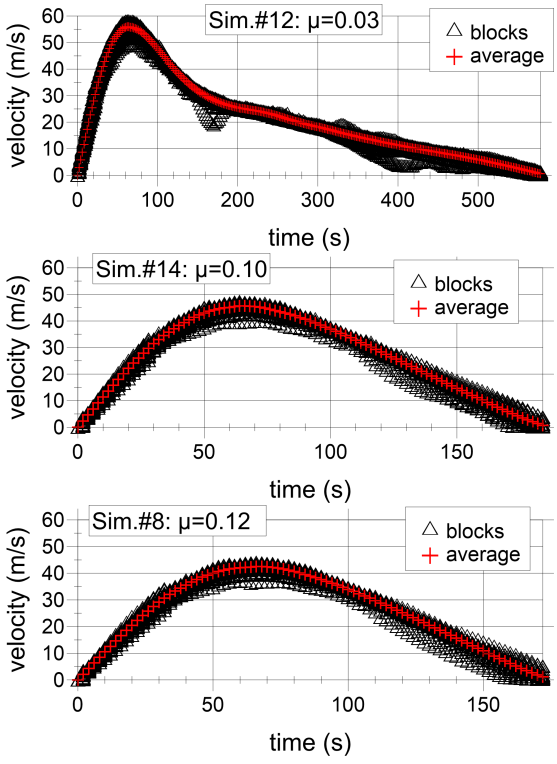

Figure 4.16: Velocities of the centres of mass of the blocks (triangles) and weighted average values (crosses) for simulations with μ equals to 0.03 (Sim. 12), 0.10 (Sim. 14), and 0.12 (Sim. 8).

4.2.5 Tuning the drag coefficients C_d and C_f

In the majority of the simulations carried out the two drag coefficients have been set at the values known to be generally valid to simulate a submarine landslide, i.e. 0.01 for the top drag coefficient C_d and 2 for the frontal drag coefficient C_f. These two parameters can be considered fixed and generally they do not represent a degree of freedom for the simulations. Nevertheless, for the sake of completeness, it was chosen to study how variations of C_d and C_f affect the simulated dynamics of the blocks.

To comment the dependence on the drag coefficients, we will compare the outcomes of simulations 15, in which C_d=0.01 and C_f=2 (Fig. 4.8), 17 in which C_d=0.001 and C_f=1 (Fig. 4.17, upper panel) and 16 in which C_d=0.001 and C_f=0.5 (Fig. 4.17, lower panel).

From the comparison of the latter figures, one can notice that varying C_d and C_f does not produce a difference in the final deposit thickness distribution, but has an effect on the run-out similar to the one observed by varying the friction coefficient. In fact, lowering the drag coefficients the whole mass travels for a longer distance.

More interesting is the time evolution of the velocity depicted in Figs. 4.9 and 4.18. For the simulations 17 and 16 one can recognise three phases as was described for simulation 15 in a previous section. Even for simulations 17 and 16 the first phase (in which the average velocity increases linearly with time) goes from t = 0 s to t =25 s. The second phase (in which the time derivate of the average velocity decreases remaining positive) ends at t =70 s and t =76 s when the average velocity reaches its maximum value (namely 56 m/s and 60 m/s) respectively for simulations 17 and 16. Thus, lowering the drag coefficients produces the effects of increasing both the peak velocity and the time at which the latter is reached.

In the third phase of the motion there is a difference as regards the concavity of the average velocity time series. In fact in both simulations 17 and 16 there is a change in the concavity that is not present in the velocity plot of simulation 15. From the instant in which the maximum velocity is reached to the instant t* (equal to 220 s and 170 s respectively for simulations 17 and 16) one can see the upward concavity, while from t* to the end of the sliding all the average velocity points lay on a straight line that has the same slope in the two simulations. It is interesting to point out that, for t=t*, the average velocity is approximately equal to 30 m/s for simulation 17 and 20 m/s for simulation 16.

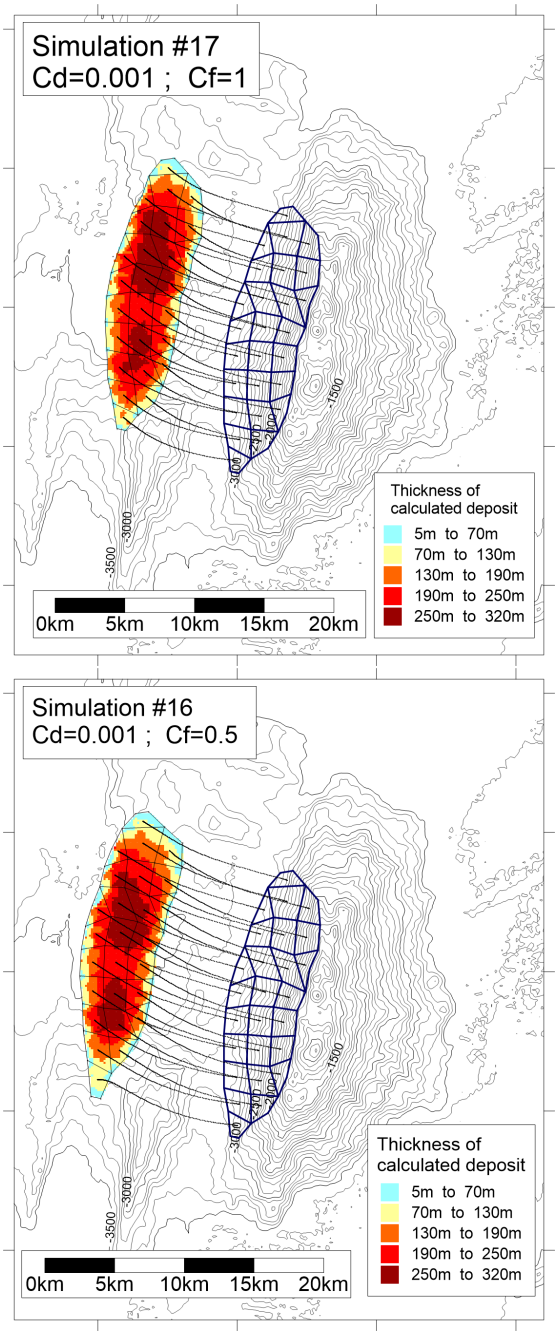

Figure 4.17: Results for the drag coefficient pairs C_d=0.001, C_f=1 (Sim. 17, upper panel) and C_d=0.001, C_f=0.5 (Sim. 16, lower panel). The simulated deposit thickness is represented in colours with superimposed the block structure at the end of the simulation (black line). The black dots represent the centres of mass of the blocks at evolving time steps. The blue grid represents the blocks at the initial time.

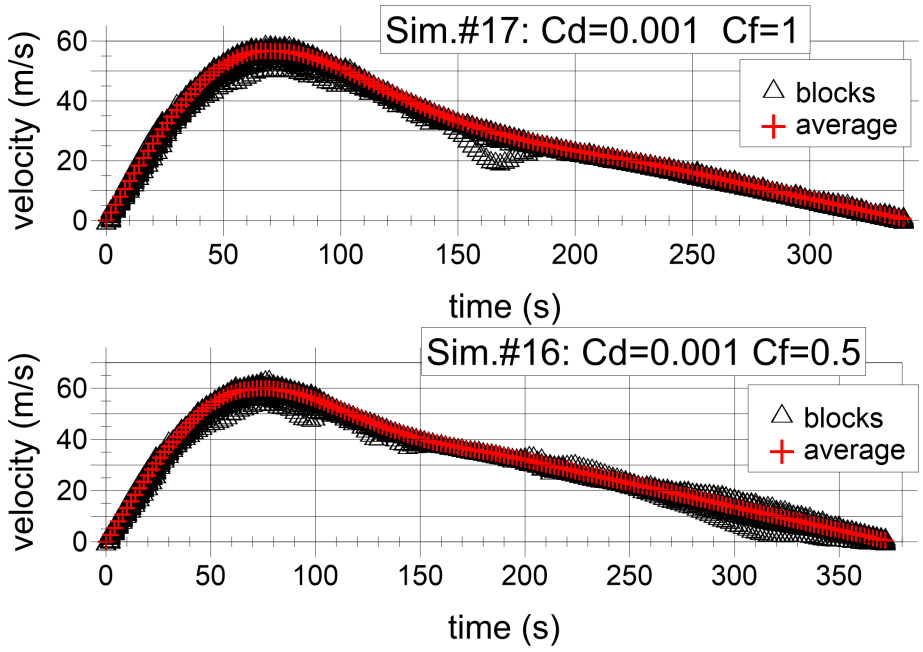

Figure 4.18: Velocities of the centres of mass of the blocks (triangles) and weighted average (crosses) for simulations with C_d=0.001, C_f=1 (Sim. 17) and C_d=0.001, C_f=0.5 (Sim. 16)

4.3 Collapse simulations for scenario 2

The simulations regarding scenario 2 are voted to compare the hypothesised deposit with the calculated one for various values of the friction coefficient μ. Therefore in all the simulations the interaction parameter λ was set to 1 (maximum value) and the drag coefficients to the usual values: C_d=0.01, C_f=2. Moreover, for the simulations regarding scenario 2, the number of blocks that represent the sliding mass is increased to the number of 106. Considering a larger number of blocks results in a better discretisation of the sliding mass but implies a greater computer demand and, therefore, a longer execution time.

As already discussed, the decision to set λ equal to 1 has the consequence for the simulation to be more prone to a numerical failure due to a block that overdeforms, which occurs more frequently when an irregular block discretisation is applied. Being the influence on the dynamics of a regular/irregular blocks structure a topic already explored, we decided to keep an irregular block division whenever it was possible, while when it was not we considered the regular block simulation's output.

The total number of simulations conducted for scenario 2 are 6. They are referred to with an increasing number that goes from 25 to 30. In the next sub-sections we will present the results obtained setting μ equal to 0.06, 0.12, 0.15, 0.18.

4.3.1 Results for the friction coefficient μ = 0.06

For simulation 25 the friction coefficient is set equal to 0.06. The result of the simulation is shown in Fig. 4.19. In the upper panel one can see the initial block division (green grid), the final thickness of the simulated mass (classed post map) and its division in blocks (black grid). We notice that the area of the deposit is similar to the initial area occupied by the mass, since the mass remains compact during sliding.

The average distance travelled by the mass is 6500 m and it is analogous to the distance travelled in the simulation for scenario 1 conducted with the same value of μ, that was 6400 m recorded in simulation 15. The two simulations present also similar thickness distributions of the deposit.

The lower panel of Fig. 4.19 is the plot of the time series for the velocities of each block (triangles) and their weighted average. The plot is similar to the one for simulation 15 depicted in Fig. 4.9. There are some differences, though: (1) in simulation 25 the peak velocity is 56 m/s while it was 52 m/s in the case of scenario 1; (2) the maximum of the average velocity is found for t = 68 s while it was found at t = 64 s for simulation 15; (3) eventually the motion lasts 254 s, while it lasted 272 s for scenario 1.

In Fig. 4.20 we depict the cross-sections taken along the lines 1 - 5 of the upper panel of Fig 4.19. The cross-sections are the ones of the current bathymetry (black line), of the sliding surface (blu line) and of the post-collapse bathymetry (output of simulation 25). The area enclosed between the blue and the black line is the cross-section of the removed material, while the one enclosed between the blu line and the orange line stands for the simulated deposit.

In all the transversal cross-sections (1 to 4) the calculated deposit exceeds the limit imposed by the current bathymetry line. In addition, cross-sections 1 to 3 show that the area of the removed material is only partially filled: a gap is still present in the region adjacent to the flank of the seamount. In cross-section 4 the gap is more marked, since the calculated deposit remains completely outside of the excavated area.

The cross-section 5 shows that the deposit fills only partially the excavated region, in fact there is no material in the southern region as already pointed out by commenting cross-section 4.

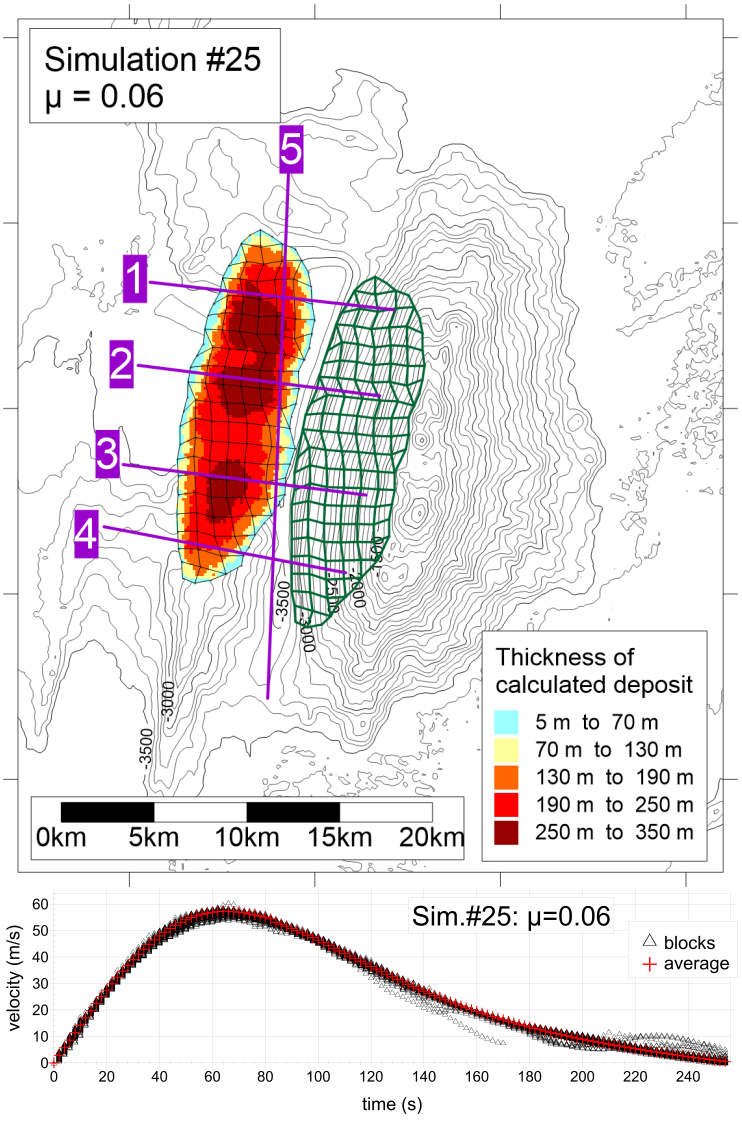

Figure 4.19: Simulation 25, relative to scenario 2, $\mu = 0.06$. The upper panel shows the thickness of the collapsed mass at the end of the simulation (colour scale), with superimposed the block structure (black line). The initial block division is represented by the green grid. Lines 1 - 5 are the ones used for the cross-sections of Fig. 4.20. The lower panel shows the time evolution of the velocity for the centres of mass of the blocks (triangles) and for their weighted average (crosses).

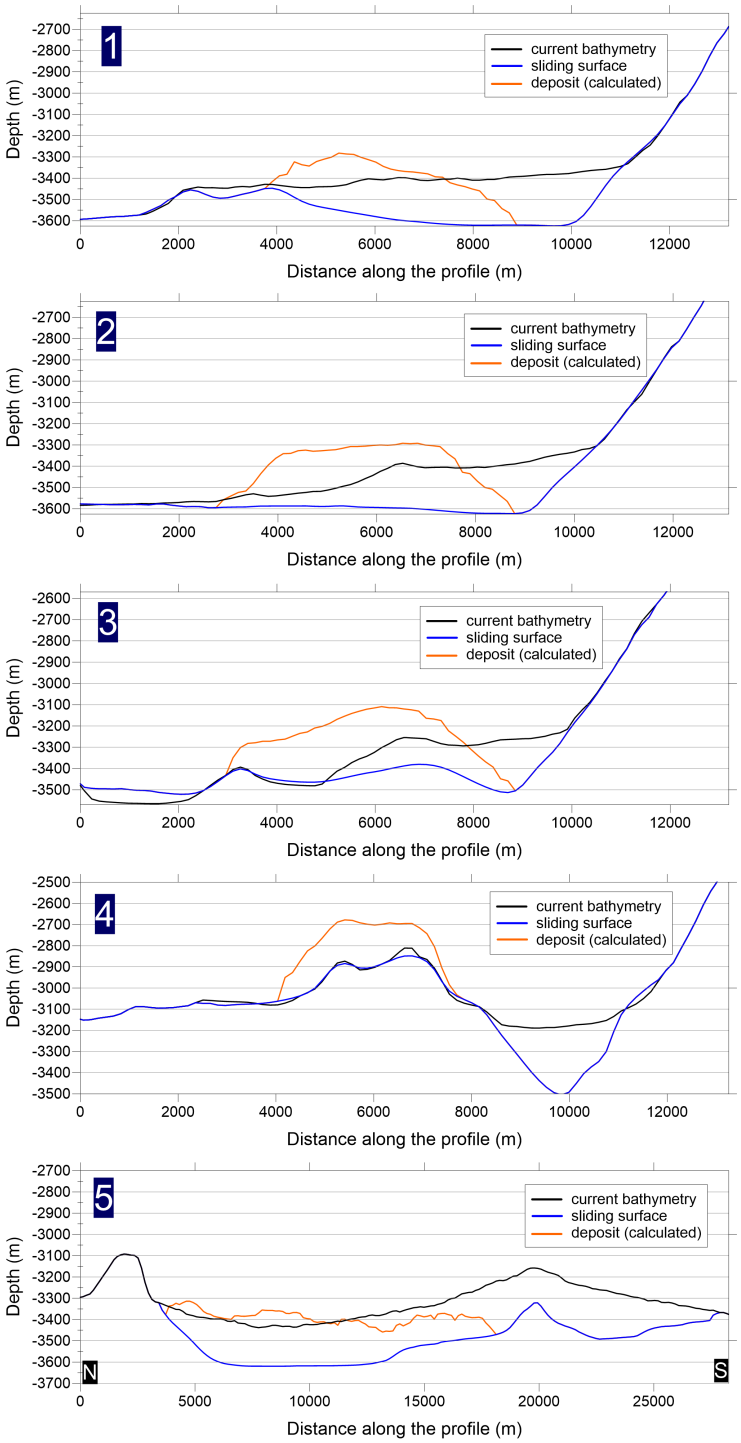

Figure 4.20: Cross-sections taken along lines 1 - 5 of Fig 4.19, relative to the simulation 25 (with $\mu = 0.06$) for scenario 2. The black lines represent the current bathymetry of the Vavilov seamount, blue lines are used to indicate the sliding surface hypothesised in section 4.1.2. The orange line stand for the cross-section of the simulated deposit.

4.3.2 Results for the friction coefficient $\mu = 0.12$

The value of the friction coefficient was set equal to 0.12 in simulation 28 for scenario 2. Therefore, simulation 28 differs from simulation 8 not for the parameters chosen but only for the scenario (excluding the already debated block division).

In the upper panel of Fig. 4.21 one can notice that even in this case the mass terminates its motion conserving its initial shape and thickness distribution, in fact the deposit is similar to the ones observed in the previous case. The average distance travelled by the blocks is equal to 4900 m (while it was 4200 m in simulation 8).

By looking at the lower panel of Fig. 4.21 one can notice that, having set $\mu = 0.12$, the sliding lasts 174 s. Therefore, it is shorter than the simulated sliding for $\mu = 0.06$ (254 s), as we expected considering the run-out.

Another value that one can read from the aforementioned plot is that the maximum value of the average velocity is equal to 48 m/s and it is reached at t = 68 s (as for simulation 25). Likewise simulation 8, for simulation 28 the sliding process does not last enough time that the average velocity presents an evident upward concavity in the third phase.

In Fig. 4.22, 5 cross-sections are shown analogous to the ones of Fig. 4.20 but relative to simulation 28, with $\mu = 0.12$. From panels 2 and 3, one can notice that the simulated deposit fills nicely the gap left by the excavation process: in cross-section 2 the calculated deposit perfectly coincides with the current bathymetry while, in cross-section 3, there is a good agreement between the deposit line and the current bathymetry.

In cross-section 1 the mass slides too far from the flank leaving a gap between the current bathymetry and the simulated one. A similar gap is seen also in the region of 5000 m of the plot. Panel 4 shows a result in agreement with what seen with a lower value of μ (panel 4 of Fig. 4.20). In fact, the mass almost overruns the excavated region.

With respect to panel 5 of Fig. 4.20, the analogous panel for the simulation with $\mu = 0.12$ shows a better overlap between the calculated deposit (orange line) and the excavated material (enclosed between the blu and the black lines). Indeed, the orange and the black lines are very similar between 4000 and 22000 m (distance along the line). Still, after the simulation the southern region presents a gap between the calculated bathymetry and the current one.

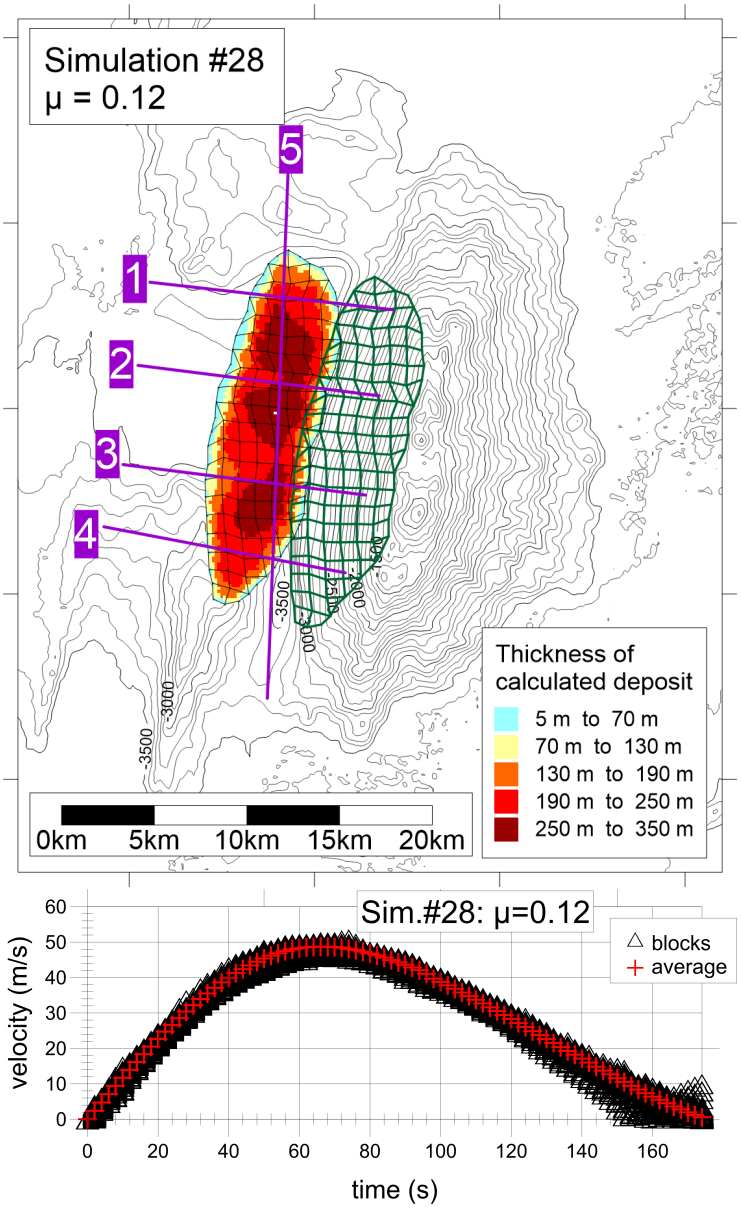

Figure 4.21: Simulation 28, relative to scenario 2, $\mu = 0.12$. The upper panel shows the thickness of the collapsed mass at the end of the simulation (colour scale), with superimposed the block structure (black line). The initial block division is represented by the green matrix. Lines 1 - 5 are the ones used for the cross-sections of Fig. 4.22. The lower panel shows the time evolution of the velocity for the centres of mass of the blocks (triangles) and for their weighted average (crosses).

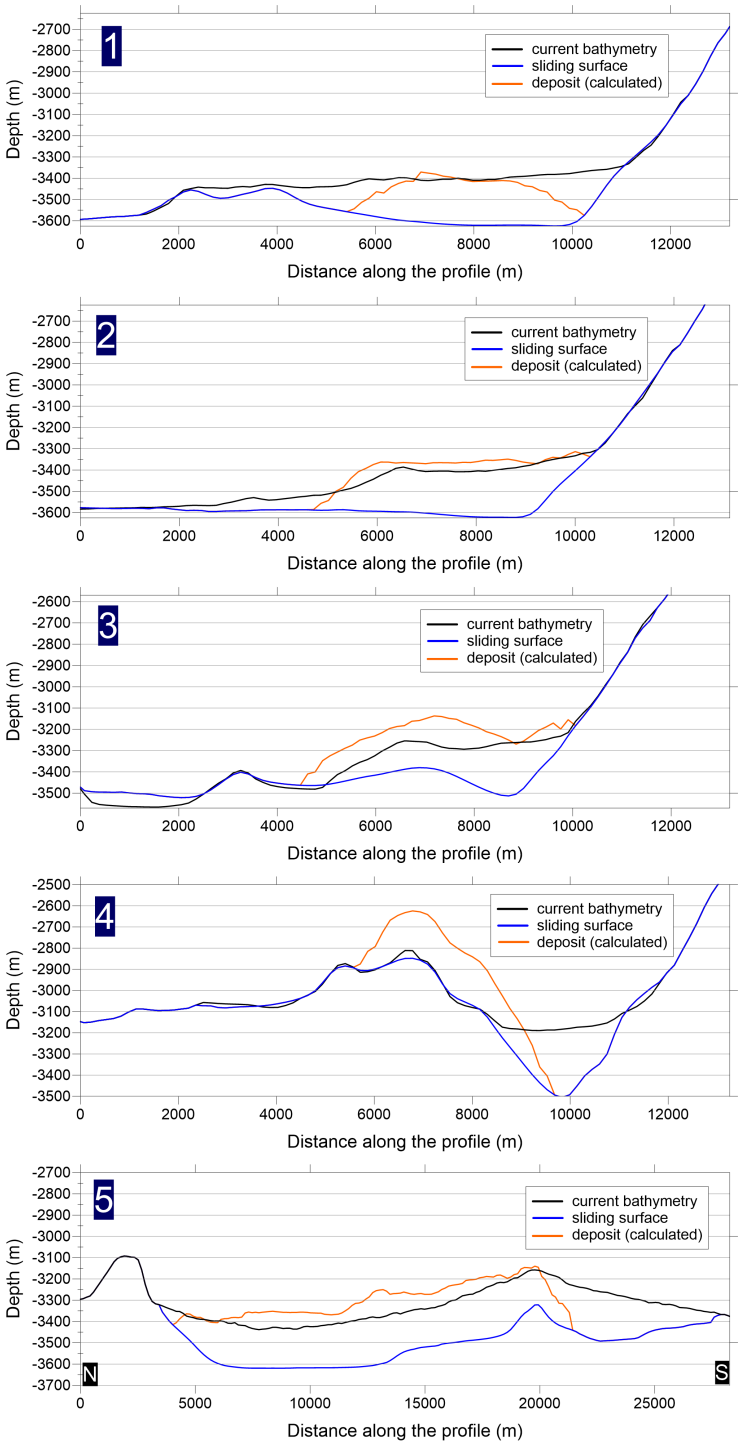

Figure 4.22: Cross-sections taken along lines 1 - 5 of Fig 4.21, relative to the simulation 28 (with $\mu = 0.12$) for scenario 2. The black lines represent the current bathymetry of the Vavilov seamount, blue lines are used to indicate the sliding surface hypothesised in section 4.1.2. The orange line stands for the cross-section of the simulated deposit.

4.3.3 Results for the friction coefficient μ = 0.15

The simulation 29 is the one relative to scenario 2 conducted after setting $\mu = 0.15$. There is not an analogous simulation for scenario 1 because $\mu = 0.15$ is outside of the range generally adopted to model submarine landslide events. However, we wanted to investigate the response of the model under higher values of μ in order to understand if such a value of the friction coefficient was more indicated for the simulation of the Vavilov collapse hypothesis.

In Fig. 4.23 we show the results of the simulation regarding its final position and thickness (upper panel) and the velocities of the centres of mass (lower panel). From these graphs one can infer that setting $\mu = 0.15$ entails an average motion length of 4150 m that lasts for 162 s, and an average maximum velocity of 44 m/s that is reached at t = 68 s. Therefore, with respect to the simulations 25 and 28 conducted with lower values of the friction coefficient, one observes that increasing μ leads to lower velocities and shorter run-outs, as was pointed out in presenting scenario 1. The plot of the lower panel of Fig. 4.21 does not show a clear upper concavity in the third phase of the motion, as already noticed for the simulation with $\mu = 0.12$.

The cross-sections of Fig.4.24 show a good agreement between the calculated post-collapse bathymetry and the current one in the region nearer the seamount of panel 1 while there is still a gap between 4000 and 7000 m along the line. Cross-sections 2 and 3 show that the deposit produced by the simulation is higher than the current sea bottom line (black) in the region closer to the seamount's flank. The gap produced by the excavation is only partially filled along the cross-section 4. Cross section 5 confirms the latter observation, being the simulated post-collapse bathymetry in disagreement with the current one from 2200 m to 2800 m. In addition, a gap between the current bathymetry and the post-collapse simulated one is seen also in the northern part of the line, while it was not present for the simulations with lower values of the sea bottom friction parameter.

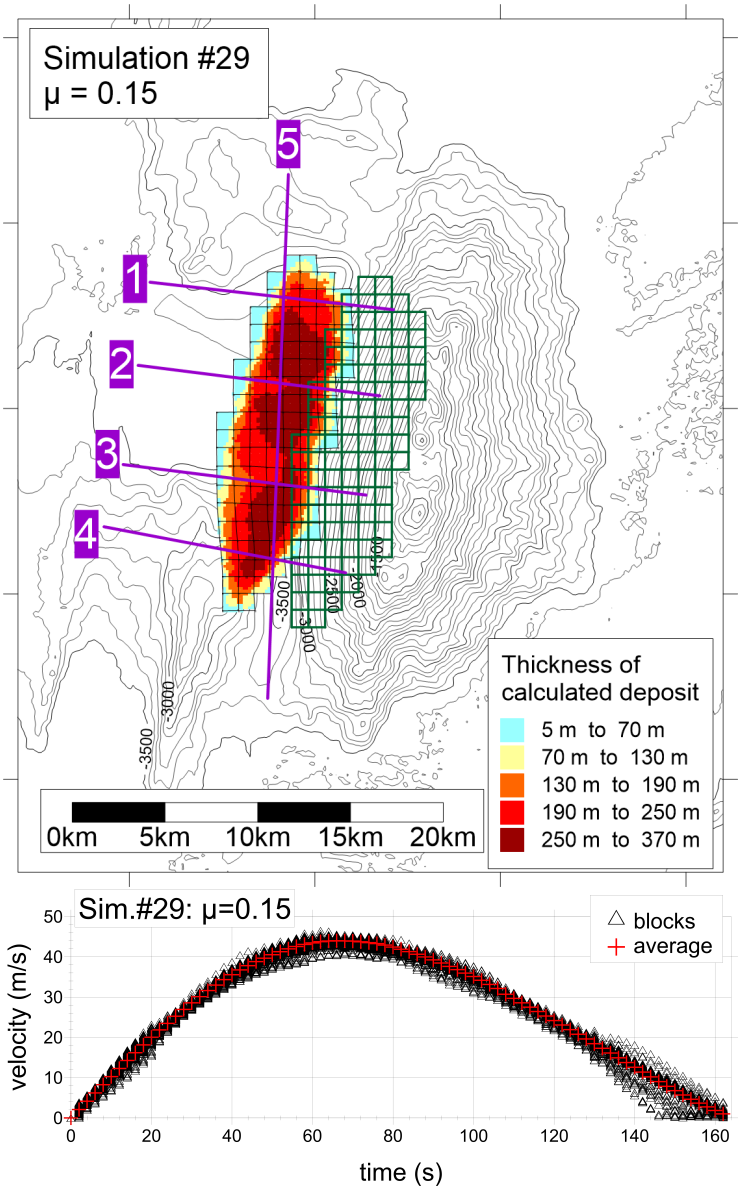

Figure 4.23: Simulation 29, relative to scenario 2, $\mu = 0.15$. The upper panel shows the thickness of the collapsed mass at the end of the simulation (colour scale), with superimposed the block structure (black line). The initial block division is represented by the green grid. Lines 1 - 5 are the ones used for the cross-sections of Fig. 4.24. The lower panel shows the time evolution of the velocity for the centres of mass of the blocks (triangles) and for their weighted average (crosses).

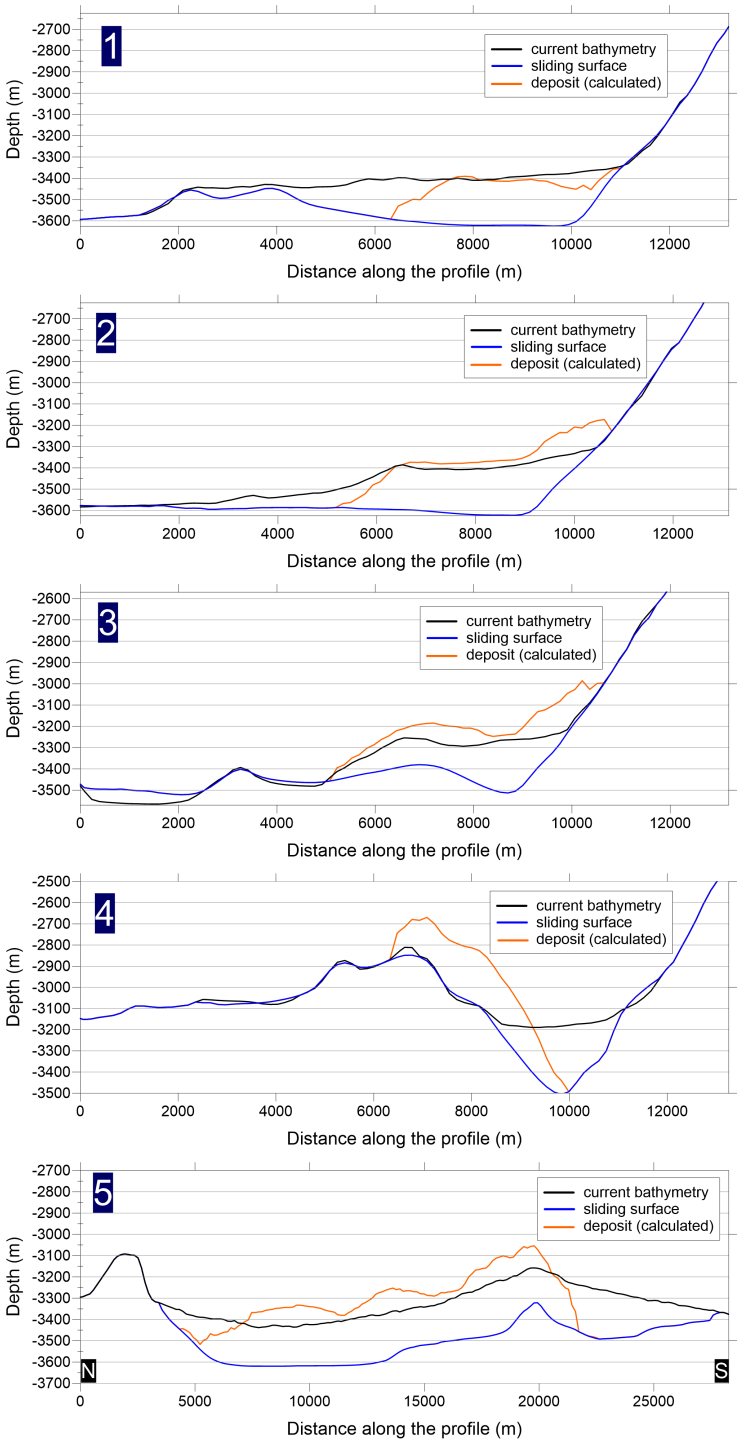

Figure 4.24: Cross-sections taken along lines 1 - 5 of Fig 4.23, relative to the simulation 29 (with $\mu = 0.15$) for scenario 2. The black lines represent the current bathymetry of the Vavilov seamount, blue lines are used to indicate the sliding surface hypothesised in section 4.1.2. The orange line stands for the cross-section of the simulated deposit.

4.3.4 Results for the friction coefficient μ = 0.18

The highest value set for the friction coefficient is 0.18 regards the simulation 30. The result shown in the upper panel of Fig. 4.25 indicates that the average distance travelled by the mass is smaller than in the previous cases. In fact here the run-out is equal to 3600 m. The lower panel of the aforementioned figure yields that also the maximum average velocity (39 m/s) and the time length of the motion (156 s) are smaller.

From the lower panel of Fig. 4.25, one can further notice that, as for the other simulations, all the blocks velocities do not significantly differ from the average value, which is a hint that the whole landslide remains compact and this is confirmed from the shape of the final deposit grid shown in the upper panel of the same figure.

The first two phases of the motion are similar to the ones observed for the previous simulations conducted on scenario 2, i.e. also for simulation 30 the slope of the average velocity starts decreasing at t = 25 s (end of the first phase) and reaches the maximum value at t = 68 s (end of the second phase). The third phase does not present any upward concavity, but a linear trend that goes from t = 106 s (when the speed is 32 m/s) to the end of the sliding.

From Fig. 4.26 one can notice that most of the mass, that is comprised between the lines 2 and 3, overpasses the current bathymetry line in the region closer to the flank. On the contrary, there is a good overlap of the black and orange line in the zone closer to the flank for the northern slice of panel 1. In panel 4, consistently with the analogous panels for the previous cases, one can notice that the mass still overruns the excavation zone leaving moreover a hole with respect to the current bathymetry.

Cross-section 5 evidences that even with a friction coefficient as high as μ = 0.18, the region comprised between the Vavilov's flank and the sea bottom high is not filled by the collapsed material. Moreover, such a value of μ enlarges the gap in the northern region as pointed out also for simulation 29.

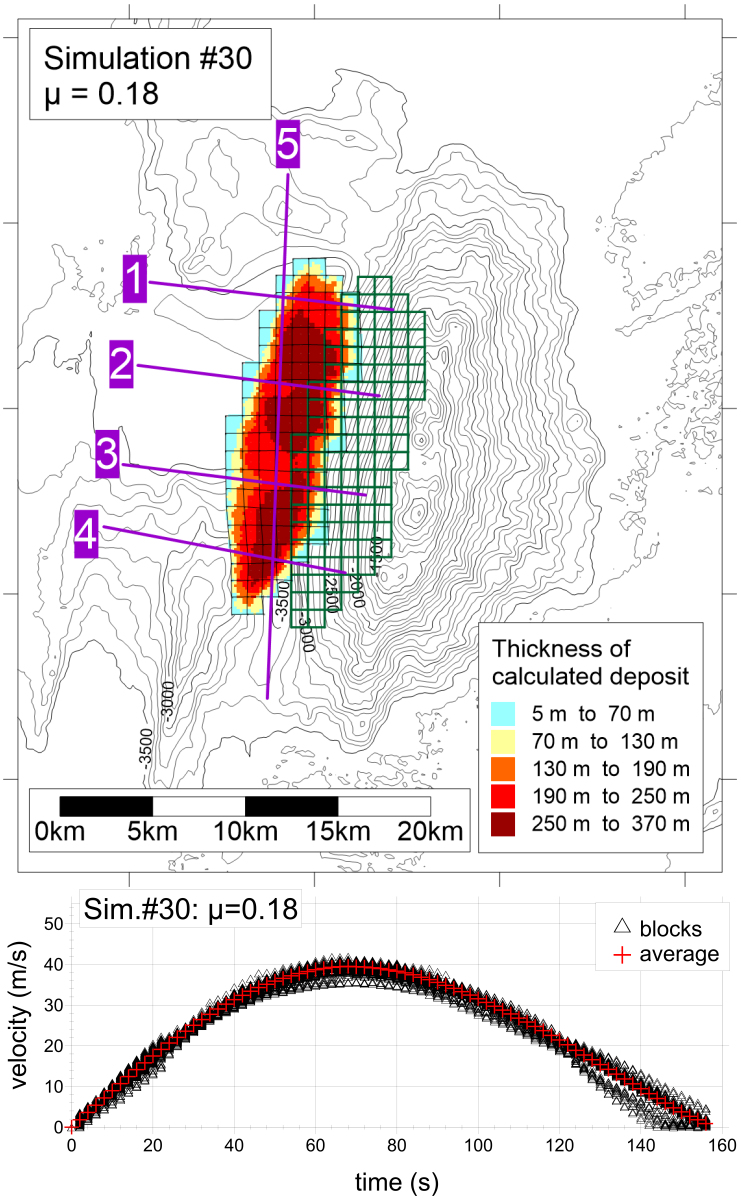

Figure 4.25: Simulation 30, relative to scenario 2, $\mu = 0.18$. The upper panel shows the thickness of the collapsed mass at the end of the simulation (colour scale), with superimposed the block structure (black line). The initial block division is represented by the green grid. Lines 1 - 5 are the ones used for the cross-sections of Fig. 4.26. The lower panel shows the time evolution of the velocity for the centres of mass of the blocks (triangles) and for their weighted average (crosses).

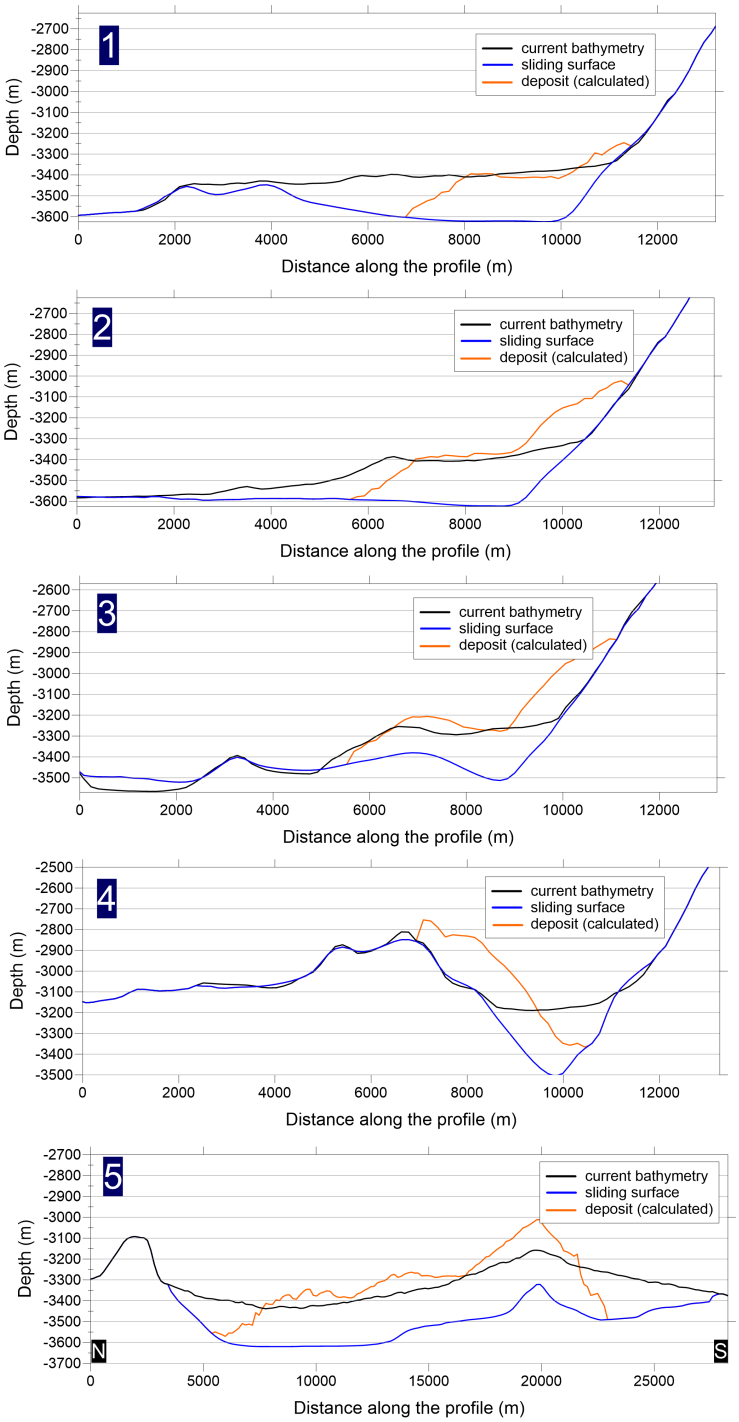

Figure 4.26: Cross-sections taken along lines 1 - 5 of Fig 4.25, relative to the simulation 30 (with $\mu = 0.18$) for scenario 2. The black lines represent the current bathymetry of the Vavilov seamount, blue lines are used to indicate the sliding surface hypothesised in section 4.1.2. The orange line stands for the cross-section of the simulated deposit.

Chapter 5

Discussion of the results and Conclusions

5.1 The influence of the parameters on the model

The results presented in the previous chapters allow us to draw some considerations on the influence of the parameters on the simulations and on the two scenarios produced with different assumed pre-collapse morphology of the Vavilov's western flank and of its surroundings. We are interested in highlighting the differences for the peak velocity results obtained by varying the parameters. In fact, the peak velocity and the initial acceleration are the most influencing parameters for the tsunami wave generation, that will be developed as the prosecution of this thesis.

We noticed that running a simulation with regular blocks instead of irregular ones has the advantage of diminishing the probability of the blocks to over-deform resulting in the simulation's stop. On the contrary, the regular blocks represent only a rough approximation of the mass at its initial position. Hence, the output of a regular-block simulation may lack accuracy in calculating the dynamical variables of the border blocks, as we saw for the southernmost block of simulation 18 (Fig. 4.7).

However, we evidenced that in general the dynamics of the blocks is the same with both types of discretisation (regular or irregular blocks). Especially we noticed that this is true for the first two phases of the motion, that are the ones that mostly affect the tsunami generation. Hence, we can conclude that an irregular block division is to prefer to the regular one. But, if the output of the irregular blocks case is not available because the code reaches a level of instability, then one may equally well consider the output concerning a regular-block discretisation, keeping however in mind that it may lack accuracy for the border blocks.

We further noticed that the number of blocks used to represent the falling mass

does not have a great influence on the dynamics. However, a finer blocks division is to prefer because, even if more computational demanding, can simulate the mass with a greater definition. This aspect was evidenced by both the overlap of the blocks' grid with the surface of rupture and the thickness distribution of the simulated deposit.

In this thesis we analysed the effects of setting different values of the interaction parameter λ. In this context, we pointed out that, as expected by the theory of the model, λ governs how much the blocks are allowed to deform. In particular, we observed that increasing λ increases the possibility for blocks to deform during sliding. We also noticed that practically no deformation took place for $\lambda = 0.5$ (Fig. 4.11). Therefore, the range of λ for which one can see a significant effect on the results goes approximately from 0.75 to 1.

In addition, we observed that varying the interaction coefficient does not affect the peak velocity nor the time it is reached. Thus, we concluded that for real cases with a topography as "simple" as the one of the western Vavilov flank, the interaction between the blocks does not affect the sliding features in the initial stage.

A further point of interest is the study of the influence of the sea bottom friction. The numerical experiments we conducted show that increasing the friction coefficient diminishes the average peak velocity and the run-out distance while does not affect the time in which the maximum velocity is reached. Recalling equation 3.12, we can understand that higher μ values imply a lower contribution of the driving gravitative term of equation 3.10. Hence we can explain the decrement of the peak velocities for increasing μ.

Another interesting aspect that we noticed by varying the friction parameter is that in simulations with long run-outs one can see an upward concavity for the average velocity. Thus, we proposed a division of the motion in three phases. It can now be explained by considering both the sliding surface topography and the resistive term. At the beginning of the motion, the blocks slide on a surface that has practically a constant slope, therefore they are subjected to an almost constant gravitational term that accelerates them downslope. In the same time, being the velocity of the blocks not so high in the first phase, the resistive term has not a great influence on the dynamics. In addition, being the surface of the Vavilov flank particularly smooth and homogeneous, the blocks "have no need" to interact. Thus eq. 3.10 yields a constant acceleration for the first phase. The resistive term becomes influent in the second phase, but its effect is mixed with the one deriving from a lower gravity component due to a flatter sliding surface. Hence, the acceleration of the blocks decreases until becoming a deceleration. In the third phase, the blocks slide on the flat region facing the Vavilov western flank. Here, they are not speeded up by gravity anymore but only decelerated by the resistive term that depends on the squared value of the velocity and by the constant friction. Thus, as the velocity decreases the resistive term becomes less influent and the blocks deceleration diminishes as indicated by the upward concavity of the average velocity.

For what regards the friction coefficient we conclude that this parameter is the one that most affects the sliding simulation. In particular, the dependency of the run-out from μ can be explored by setting this parameter equal to a value for which the simulated deposit is located in agreement with the observed one. Clearly this operation is well-founded for those cases where the deposit is observed.

Later, we tested the output of simulations by varying the drag coefficients. The results yielded that tuning these parameters produced effects similar to the one observed by varying the friction coefficient. Hence, to limit the number of degrees of freedom of the simulation, we decided to set them equal to the usual values adopted for the submarine landslides, i.e. C_d=0.01 and C_f=2.

Further, it is interesting to point out that the linear behaviour of the velocity trend in the last phase of the motion for the simulation conducted with lower drag values can be interpreted invoking the aforementioned eq. 3.10. In fact, the long run-out of these simulation makes the mass to slide on a flat surface for a long time. Hence, the linear trend observed tells us that setting C_d=0.001, C_f=1 or 0.5 is equivalent to neglect the resistive term for velocities respectively lower than 20 m/s and 30 m/s.

5.2 The scenarios outcomes

While presenting the two scenarios studied in this thesis, we stated that the simulations conducted for scenario 1 could be considered a preparatory work for the development of the collapse for scenario 2. In fact, developing scenario 1 has brought to the estimate of the volume of the collapsed material, based on the volume that seems missing from the Vavilov's flank, namely 18.5 km^3. This figure constituted a hint for the excavation of the region facing the western side. However, the guideline followed for the excavation was to lower the western abyssal plain making it to lie at the same depth as the eastern one. The removed volume (16.8 km^3) to get the depth equalisation is consistent with the one added on the flank, and this reinforces the hypothesis that the western abyssal plane was originated by one-episode deposition of material coming from the western flank of the Vavilov seamount and by subsequent erosional smoothing of highs and redistribution of rocks due to the action of sea bottom currents.

Having considered this hypothesis worth of deepening, we conducted a series of simulations for the flank collapse voted to find out the value of the friction coefficient μ for which the simulated deposit lies in the region hypothesised to be the observed deposit. In conformity with results obtained by changing the friction coefficient for scenario 1, we observed that increasing μ reduces the run-out making the mass to stop closer to the flank.

The cross-sections produced for the simulations conducted for μ equal to 0.06, 0.12, 0.15, 0.18 (Figs. 4.20, 4.22, 4.24 and 4.26) show that the southern region of the hypothesised deposit is only partially filled even with values of μ considered high. This

evidence can be explained by the fact that the southern region has been lowered less than the northern one because in the first instance explored in this thesis we connected the sliding surface with the sea-bottom high located SW of the seamount. Therefore, the southernmost blocks of scenario 2 slide on a surface whose slope changes less abruptly than the one for the northern blocks. Because of this, when blocks reach the flat plain, the southernmost blocks conserve a greater amount of their kinetic energy that allows them to climb up the sea-bottom high overpassing the excavated area.

On the contrary, for large μ values (namely 0.15 and 0.18) the mass stops too early in the central region where it is located most of the volume, as depicted in the graphs of cross-sections 2 and 3. In the central region of the collapsing mass, the better agreement between the hypothesised deposit and the simulated one is found for $\mu = 0.12$ of simulation 28.

By comparing simulations conducted with the same parameter set on the two scenarios (i.e. simulations pairs 15 - 25, and 8 - 28), we observed that the average peak velocity for scenario 2 is greater and it is reached later than for the other scenario. This result is explained by the fact that the portion of the sliding surface that lies on the flank of the seamount and that is characterised by a strong steepness, is more extended in scenario 2 because of the excavation made.

5.3 Conclusions

This work thesis is focused on studying the dynamics of the Vavilov seamount collapse hypothesis. This hypothesis needs to be investigated because submarine landslides may be events that generate violent tsunami. In addition, this seamount presents a great asymmetry between its western and eastern flanks. We discussed the reasons that may have brought to a similar shape of the seamount and we concluded that the detachment of a large single mass from the western flank is a possible explanation.

In this thesis two different scenarios for the western pre-collapse flank were presented. In the first one the flank has been reshaped adding the mass that seems missing. While in scenario 2 the observed difference between the depth of the two abyssal planes west and east of the Vavilov seamount has been considered as being due to the deposition of the collapsed material. Hence, the deposit was removed and the flank reshaped. The accordance between the volumes of added and removed material enforces the hypothesis of the collapse.

To simulate the dynamics of the submarine landslides in both scenarios we used the model UBO-BLOCK2 that considers the failure as the sliding of many interacting blocks, whose motion is governed by gravity, friction, drag and interaction forces. The influence of these forces is governed by a set of parameters.

The simulations conducted on scenario 1 brought to the conclusion that the parameter most affecting the simulation in its initial phase is the sea bottom friction coefficient.

With this in mind, we ran the model UBO-BLOCK2 by varying values of μ for scenario 2. A comparison between the simulated deposit with the material considered to be derived by the flank's collapse, induced us to conclude that the best agreement of the latters is obtained for $\mu = 0.12$, in accordance with the plausibility range of this parameter.

Moreover, it is worth to remark that the available seismic data for the Vavilov zone cover the crucial area, though they have a poor resolution (see Chapter 2). Indeed, it seems that they are such to intersect the region of the hypothesised mass failure west of the Vavilov. As we explained, the discontinuity for the regular sedimentary pattern of the seismic profiles (Fig. 2.5) is located just to the feet of the seamount and can be interpreted as the presence of rocky material detached from the flank. Though the disturbed region can be explained differently, the hypothesis of a collapse with a limited run-out seems to be the most reasonable explanation. This poses further important constraints to our modelling. In our simulations of scenario 2, the run-out was short enough in the cases where the highest values of the bottom friction were used, i.e. $\mu = 0.12 - 0.18$. Since these values are to be preferred also in view of the best fit between observed and computed deposit, it follows that there are at least three important hints to support the hypothesis of a collapse of the western flank of the Vavilov seamount, which is relevant since they are proposed for the first time in the scientific literature. To summarise these are: 1) similarity between the volume of the missing seamount and the volume of the sediment removed to equalise the depth of the abyssal plains; 2) fit between the simulated deposit and assumed observed deposit; 3) short run-out distance for the collapsing material compatible with the known seismic lines.

References

[1] Abadie, S., Morichon, D., Grilli, S., and Glockner, S. Vof/navier-stokes numerical modeling of surface waves generated by subaerial landslides. *La Houille Blanche 1* (2008), 21–26.

[2] Bortolucci, E. *Modelli dinamici di frane e dei maremoti indotti*. PhD thesis, Università degli studi di Bologna, 2001.

[3] Caratori Tontini, F., Cocchi, L., Muccini, F., Carmisciano, C., Marani, M., Bonatti, E., Ligi, M., and Boschi, E. Potential-field modeling of collapse-prone submarine volcanoes in the southern Tyrrhenian Sea (Italy). *Geophysical Research Letters 37* (2010), L03305.

[4] Cruden, D., and Varnes, D. Landslide types and processes. *In: Turner, A.K., Schuster, R.L. (Eds.), Landslides: investigation and mitigation. National Academy Press,Washington, D.C 247* (1996), 36–75.

[5] EMODnet. European Marine Observation and Data Network. `http://www.emodnet-bathymetry.eu`, 2018. [Online, accessed November 21, 2018].

[6] Gamberi, F., Marani, M., Landuzzi, V., Magagnoli, A., Penitenti, D., Rosi, M., Bertagnini, A., and Roberto, A. D. Sedimentologic and volcanologic investigation of the deep Tyrrhenian Sea: preliminary result of cruise VST02. *Annals of Geophysics 49*, 2-3 (2009).

[7] Hampton, M. A. The role of subaqueous debris flow in generating turbidity currents. *Journal of Sedimentary Research 42*, 4 (1972), 775–793.

[8] Hungr, O., Evans, S., Bovis, M., and Hutchinson, J. Review of the classification of landslides of the flow type. *Environmental & Engineering Geoscience 7* (2001), 221–238.

[9] Kastens, K., Mascle, J., Auroux Christian, A., Bonat ti, E., Broglia, C., Channell, J., Curzi, P., Emeis, K., Glacon, G., Hasegawa, S., Hieke, W., Mascle, G., Fw, M., McKenzie, J., Mendelson, J., Mueller, C., Rehault Jean, P.,

Robertson, A., Sartori, R., and Torii, M. ODP Leg 107 in the Tyrrhenian Sea: Insights into passive margin and back-arc basin evolution. *Geol. Soc. Am. Bull. 100* (1988), 1140–1156.

[10] Marani, M., and Gamberi, F. Distribution and nature of submarine volcanic landforms in the Tyrrhenian Sea: the arc vs the backarc. *Memoir Carta Geologica D'Italia 64* (2004), 109–126.

[11] Marani, M., Gamberi, F., Ivanov, M., and Ship-Board Party. Introduction and main objectives of TTR-12 Leg IV - Tyrrhenian Sea. *IOC, Technical Series 67* (2003), 72–90.

[12] N. Hutchinson, J. A sliding–consolidation model for flow slides. *Canadian Geotechnical Journal 23* (1986), 115–126.

[13] Pierson, T., and Costa, J. A rheologic classification of subaerial sediment-water flows. *Debris flows/avalanches 7* (1987).

[14] Robin, C., Colantoni, P., Gennesseaux, M., and Rehault, J. Vavilov seamount: A mildly alkaline Quaternary volcano in the Tyrrhenian Basin. *Marine Geology 78*, 1 (1987), 125 – 136.

[15] Savage, S. B., and Hutter, K. The dynamics of avalanches of granular materials from initiation to runout. Part I: Analysis. *Acta Mechanica 86*, 1 (1991), 201–223.

[16] Savelli, C. Two-stage progression of volcanism (8-0 Ma) in the Central Mediterranean (Southern Italy). *Journal of Geodynamics - J GEODYNAMICS 31* (2001), 393–410.

[17] Tinti, S., Bortolucci, E., and Vannini, C. A block-based theoretical model suited to gravitational sliding. *Natural Hazards 16*, 1 (1997), 1–28.

[18] USGS. U.S. Geological Survey. `http://landslides.usgs.gov/html_files/nlic/nlicmisc.html`. [Online, accessed February 14, 2019].

[19] Varnes, D. Slope movement types and processes. *Landslides: Analysis and control: National Research Council, Washington, D.C., Transportation Research Board Special Report 176* (1978), 11–33.

[20] Yavari-Ramshe, S., and Ataie-Ashtiani, B. Numerical modeling of subaerial and submarine landslide-generated tsunami waves—recent advances and future challenges. *Landslides* (2016).

[21] Zaniboni, F. *Modelli numerici di evoluzione di frane con applicazione a casi di frane tsunamigeniche subaeree e sottomarine*. PhD thesis, Università degli studi di Bologna, 2004.

[22] Zaniboni, F., Armigliato, A., and Tinti, S. A numerical investigation of the 1783 landslide-induced catastrophic tsunami in Scilla, Italy. *Natural Hazards 84*, 2 (2016), 455–470.

[23] Zaniboni, F., and Tinti, S. Numerical simulations of the 1963 Vajont landslide, Italy: Application of 1D Lagrangian modelling. *Natural Hazards 70* (2014).